





RESEARCH ARTICLE

10.1029/2020JB019770

Temporal Modulation of the Local Microseism in the North Sea

D. Becker¹ , L. Cristiano^{2,3}, J. Peikert², T. Kruse², F. Dethof¹, C. Hadziioannou¹ , and T. Meier²

¹Institute of Geophysics, Centre for Earth System Research and Sustainability (CEN), Universität Hamburg, Hamburg, Germany, ²Department of Geosciences, Christian-Albrechts-Universität zu Kiel, Kiel, Germany, ³Now at GFZ German Research Centre for Geosciences, Potsdam, Germany

Key Points:

- At an island in the marginal North Sea, we observe strong local primary and secondary microseism at shorter periods than remote microseism
- Local microseism exhibits a strong tidal modulation and high horizontal to vertical (H/V) ratios in the primary microseism signal
- The source region of the tidal-modulated local microseism seems to migrate in sync with the progression of the ocean tides

Supporting Information:

- Supporting Information S1

Correspondence to:

D. Becker,
dirk.becker-2@uni-hamburg.de

Citation:

Becker, D., Cristiano, L., Peikert, J., Kruse, T., Dethof, F., Hadziioannou, C., & Meier, T. (2020). Temporal modulation of the local microseism in the North Sea. *Journal of Geophysical Research: Solid Earth*, 125, e2020JB019770. <https://doi.org/10.1029/2020JB019770>

Received 13 MAR 2020

Accepted 4 SEP 2020

Accepted article online 7 SEP 2020

Abstract Primary and secondary microseism originating in the world oceans and peaking at around 14 and 7 s, respectively, characterize the Earth's background noise in that frequency range. Microseism generated in marginal seas with partly shorter periods and higher spatial and temporal variability is less studied and requires stations in immediate proximity to the source to be observed. Such studies can help to elucidate the exact microseism generation areas and mechanisms in a constrained area. We analyze 15 years of broadband data recorded at the seismic station on Helgoland island in the marginal North Sea. In addition to remote primary (RPM) and secondary microseism (RSM) originating in the North Atlantic, we observe strong and dominant local secondary microseism (LSM) with on average higher frequencies above 0.2 Hz, in accordance with shorter wave periods of about 4–8 s in the shallow North Sea. During times with low RSM activity we observe local primary microseism (LPM) at frequencies in agreement with local ocean wave periods. The higher horizontal to vertical (H/V) ratio of LPM with respect to LSM indicates a major non-Rayleigh wave contribution. LSM and LPM show a strong modulation with local semidiurnal ocean tides and microseism energy maxima preceding the water level maximum by 2.5 and 1.5 hr, respectively. This time shift might be influenced by stronger currents during rising than falling tides. Active sources of tide-modulated microseism migrate along the North Sea coast in sync with the ocean tidal signal as evidenced by comparison of LSM maxima at stations distributed along the coast.

Plain Language Summary Ocean sea waves cause seismic waves in the solid earth. These seismic waves have either the same period or half that period. They are caused by interaction of water waves with shallow seafloor structures or the interference of waves with equal period and opposite propagation directions, respectively. The period of ocean waves depends, among other factors, on the size of the water body. A smaller water body causes shorter wave periods. At an island station in the North Sea, a marginal sea of the North Atlantic, we observe simultaneously seismic wave energy generated nearby in the North Sea and far away in the North Atlantic. The North Atlantic in general generates seismic waves with longer periods. We observe seismic waves with the period and half the period of water waves in the North Sea. In addition, a modulation of the locally generated seismic wave energy with ocean tides is observed. The sources of this tidal-modulated energy move with the tidal front. This is interesting, as the exact conditions necessary to generate these seismic waves are not well understood. Our station location in direct vicinity to the generation area allows for the novel observations presented here.

1. Introduction

The global ambient noise field in the frequency band below 1 Hz is dominated by two distinct amplitude peaks (McNamara & Buland, 2004; Peterson, 1993). These are the so called primary (PM) and secondary microseism (SM) peaks (see Table 1 for a list of abbreviations used in the paper). Distinct generation mechanisms for PM and SM are suggested based on the excited frequencies and the dominant wave frequencies in the ocean (Ardhuin, 2018; Hasselmann, 1963; Longuet-Higgins, 1950). SM with a peak at about 0.15 Hz is the dominant noise source in the frequency range between 0.03 and 1 Hz and can be recorded globally. It is caused by the superposition of ocean waves with nearly opposing directions and equal frequencies (Ardhuin et al., 2015; Longuet-Higgins, 1950) that cause a pressure fluctuation in the water column. The amplitude of the generated SM is modulated by water depth (Kedar et al., 2008). Source regions of SM have been observed near the coast due to the reflection of incoming ocean waves at the shore (Bromirski & Duennebieber, 2002; Sutton & Barstow, 1996; Traer et al., 2008) and less frequently in open water locations

©2020. The Authors.

This is an open access article under the terms of the Creative Commons Attribution License, which permits use, distribution and reproduction in any medium, provided the original work is properly cited.

Table 1
Abbreviations Used in This Paper

Acronym	Full name/explanation	Frequency range (Hz)
PM	Primary microseism/microseism with the frequency of causative ocean waves	~0.04–0.2 (source dependent)
SM	Secondary microseism/microseism with double the frequency of causative ocean waves	~0.08–0.5 (source dependent)
LM	Local microseism/microseism with frequencies above 0.2 Hz (SPSM in former studies)	>0.2
LPM	Local primary microseism/primary microseism generated in the vicinity of the recording station	~0.085–0.2
LSM	Local secondary microseism/secondary microseism generated in the vicinity of the recording station	~0.17–0.5
RPM	Remote primary microseism/primary microseism generated at larger distance of the recording station (here: Northern Atlantic)	~0.04–0.1
RSM	Remote secondary microseism/secondary microseism generated at larger distance of the recording station (here: Northern Atlantic)	~0.08–0.2
PMB	PM frequency band/frequency band between 0.03 and 0.08 Hz used for data analysis	0.03–0.08
SMB	SM frequency band/frequency band between 0.08 and 0.2 Hz used for data analysis	0.08–0.2
LMB	LM frequency band/frequency band between 0.2 and 1 Hz used for data analysis	0.2–1
SWH	Significant wave height—Mean value of the upper third of all measured wave heights in a defined time interval	n.a.

Note. While LPM, LSM, RPM, and RSM describe different phenomena, PMB, SMB, and LMB describe specific frequency bands used for analysis irrespective of the phenomena observed within them.

due to the specific wave behavior in the center of a cyclone (Longuet-Higgins, 1950). The time-variable source terms of ocean microseism can be obtained by combining the modeled sea state as, for example, given in WAVEWATCH III® models (IFREMER, National Oceanic and Atmospheric Administration [NOAA]) with the bathymetry of the ocean (Hillers et al., 2012).

PM has the same frequency as the causative gravity ocean waves, peaks at about 0.07 Hz globally and is caused by the shoaling of ocean waves propagating along a sloping bottom (Ardhuin et al., 2015). Thus, the generation region of PM is generally close to shore or in shallow water regions. Numerous studies indicate that sources of SM and PM are often collocated (e.g., Cessaro, 1994; Nishida et al., 2008) although their energy ratios indicate azimuthal variability, presumably caused by the distinct radiation patterns of both microseism mechanisms (Juretzek & Hadziioannou, 2017). PM amplitudes are smaller than those of SM by orders of magnitude as also shown in global noise models (Peterson, 1993). However, due to the long wavelengths of PM and the resulting low attenuation with distance, the PM signal is also recorded globally. Close to the shore, an additional microseismic signal with higher frequencies (>0.2 Hz) is observed. It is often strongest in the period range 0.3–1 Hz, quickly decays with distance and is sometimes called short-period secondary microseism (SPSM; Chen et al., 2011). This component has been observed in Antarctica, offshore Australia, and offshore Taiwan (Cannata et al., 2019; Chen et al., 2011; Gal et al., 2015). The SPSM shows a high correlation with local sea state (Cannata et al., 2019), and for this reason we will term it local microseism (LM) in this paper.

Ocean wave frequencies are controlled by the duration of the maximum sustained wind speed and length of fetch (the distance that the wind is able to travel unobstructed over the ocean surface, Bretschneider, 1959; Pierson & Moskowitz, 1964). For open oceans with unobstructed fetch, smaller wave frequencies are expected, while the situation in marginal seas might be more complex and frequencies are generally higher. Furthermore, low-frequency ocean gravity waves that can travel over long distances in the oceans often do not enter marginal seas. Because ocean wave spectra are spread out over a finite frequency range and are modified along the wave propagation path due to attenuation and wave reflection/refraction (Kedar et al., 2008), a frequency overlap between different microseism sources (e.g., open ocean vs. marginal sea) is possible.

The different generation mechanisms of PM and SM influence the expected ratio of Love-to-Rayleigh wave excitation and thus the amplitude ratio of the horizontal to vertical components (H/V ratio) of the microseismic wavefield. PM contains considerable or even dominant contributions from horizontally polarized Love waves (Friedrich et al., 1998; Juretzek & Hadziioannou, 2016; Lin et al., 2008; Nishida et al., 2008) and thus an H/V-ratio often considerably larger than 1. On the other hand, the generation mechanism of SM mainly supports the generation of Rayleigh waves and thus a lower H/V ratio due to the absence of Love waves

(Longuet-Higgins, 1950). In addition, the exact H/V ratio of the microseismic wavefield also depends on the velocity distribution below the recording station as this influences the ellipticity of the Rayleigh waves (Tanimoto & Alvizuri, 2006) and on the attenuation of the Rayleigh and Love waves along the path from the source region to the station.

Apart from the strength of nearby or remote storm systems and the subsequent wave action, the microseismic wavefield can also be modified by ocean tides as suggested by several studies (Beucler et al., 2015; Dolenc et al., 2005; Young et al., 2013). For stations recording the North Atlantic microseism wavefield, Beucler et al. (2015) find a strong correlation between high tides of the ocean and the microseism energy over a large spectral bandwidth, except between 0.2 and 0.4 Hz—their so-called SPSM. They suggest that deep-ocean generated SPSM dominates the energy balance in the frequency range between 0.2 and 0.4 Hz.

For the MOBB seismic broadband station at the California coast, Dolenc et al. (2005) find an in-phase modulation of ocean infragravity waves with the tidal signal. These low-frequency infragravity waves are locally generated by higher-frequency ocean waves. Young et al. (2013) observe a strong tidal modulation in the infragravity frequency range (0.01–0.03 Hz) for stations within 100 m of the waterline. Maximum energy is recorded during high tide except for a station on Hawaii where a 50° phase shift is observed. For PM frequencies, they observed a strong tidal modulation for most of their sites (except for Australasian cliffs) with maximum energy at high tide with the exception of Hawaii that showed a 20° phase shift. Tidal modulation in the SM frequency band (SMB) is considerably less pronounced and explained by frequency overlap with tidally modulated PM (Young et al., 2013).

In this study, we use 15 years of continuous three-component broadband data to investigate the long-term amplitude variations of the LM noise field as recorded at seismic Station HLG on the island of Helgoland, in the marginal North Sea. Helgoland is located in the German Bight, the southeastern portion of the North Sea. We correlate the microseism data with time series of significant wave height (SWH), water level, and air pressure to identify possible generation regions (local vs. remote) and mechanisms (primary vs. secondary) of the microseism signals. Furthermore, the H/V ratio and the tidal modulation of the microseism signals are analyzed. We also compare the observations at Helgoland to nearby coastal seismological stations.

2. Study Region

The island Helgoland is located at a distance of about 50 km from the shoreline (Figures 1 and 2) in a continental shelf setting with shallow bathymetry. Maximum water depths around Helgoland do not exceed 60 m and are generally shallower than 30 m with little topography (Figure 2).

The microseism wavefield recorded in this region is dominated by sources in the North Atlantic and the North Sea as suggested by former studies (e.g., Essen et al., 1999; Grevemeyer et al., 2000). The averaged dominant period of ocean waves in the North Atlantic (west of Norway, Gulf of Biscay, and west of Ireland) obtained from NOAA WAVEWATCH III® hindcasts (ftp://polar.ncep.noaa.gov/pub/history/waves/multi_1), based on input wind and ocean-ice fields and the local bathymetry (Chawla et al., 2013; Tolman, 2009), shows an annual modulation with longer periods of about 12–13 s during boreal winter and less than 10 s during boreal summer. The occurrence of stronger and more extended storm systems in the northern winter is responsible for this modulation. The resolution of the global sea state model used in this study is 30 × 30 arc min, while the underlying bathymetric grid in the North Sea and the adjacent North Atlantic has a resolution of 8 × 4 arc min in coastal areas and 15 × 10 arc min further offshore. Average periods close to Helgoland are rather constant with about 5 s year-round (Figure 1). However, single events can cause significantly larger dominant wave periods of up to 20 s in the Atlantic Ocean and 12 s in the North Sea. This would result in dominant SM frequencies of 0.1–0.2 Hz for sources in the North Atlantic (remote secondary microseism—RSM) and about 0.17–0.5 Hz for sources in the North Sea (local secondary microseism—LSM). The corresponding PM frequencies would be 0.05–0.1 Hz (remote primary microseism—RPM) and 0.085–0.2 Hz (local primary microseism—LPM), respectively (Table 1).

All studied WAVEWATCH III® hindcast grid points in Figure 1 also show a strong variability of the dominant frequency of ocean waves on short timescales of a few days or even shorter. This variability is caused by the intensification and weakening of single or multiple storm systems, and its effect on the averaged

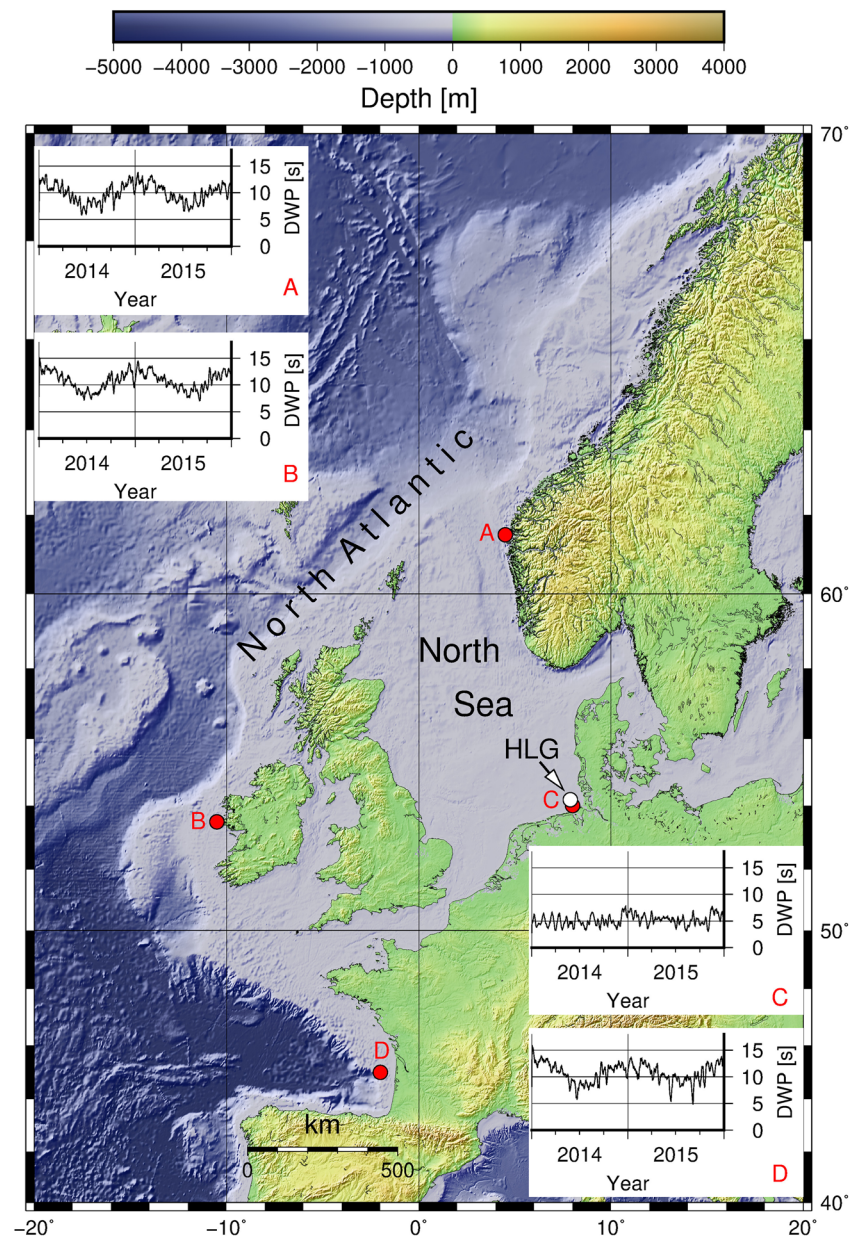


Figure 1. Bathymetry of the North Atlantic and the North Sea. Red dots indicate grid points of the WAVEWATCH III® hindcast for which the average dominant ocean wave period during 2014–2015 is given in the respective insets. Original data with 3-hr resolution were smoothed with a 56 point (i.e., 1 week) moving average and resampled to weekly values.

time profiles is visible in the smoothed time series presented for specific grid points in Figure 1 by slight deviations from the longer-term average.

The North Sea in the region of the German Bight is subject to considerable ocean tides (Figure 2). The tidal range at Helgoland is generally around 3 m with higher values during storm activity. Ocean tides in the North Sea progress from west toward the northeast in a counterclockwise fashion (Figure 2). The exact timing is influenced by the presence of off-coast islands and the extremely low bathymetry in the regions of the tidal mud flats (Wadden Sea). The tidal signal needs round about 2 hr to travel along the North Sea coast from the border between the Netherlands and Germany close to buoy RZGN1 to the border between Germany and Denmark north of the island of Sylt (Figure 2).

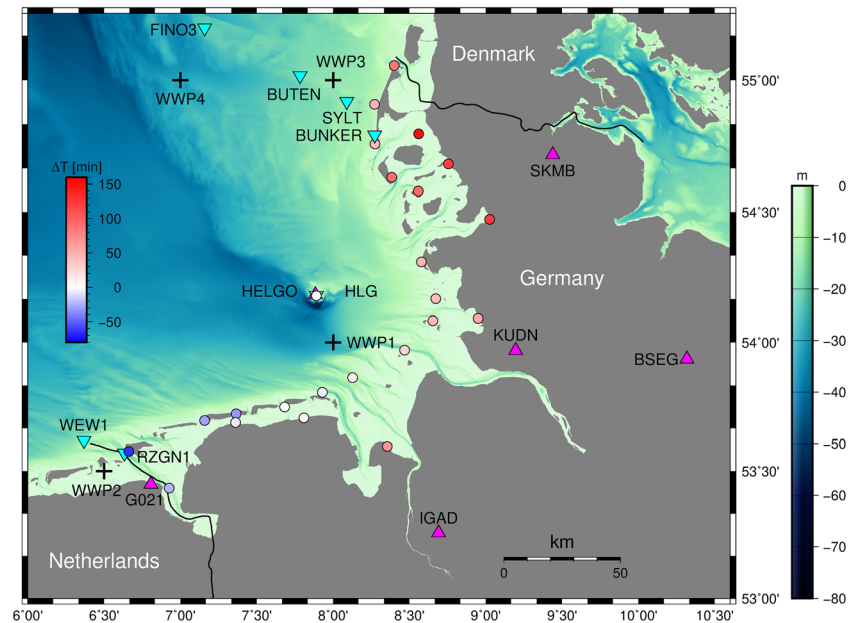


Figure 2. Bathymetry of the North Sea in the German Bight around Helgoland. Magenta triangles indicate locations of seismic stations, circles sea level gauge stations with color coding indicating the time lag (in minutes) in the ocean tidal signal relative to Helgoland. Negative times indicate earlier and positive times later maxima of the tide. Inverted cyan triangles indicate locations of buoys with sea state information and black crosses locations of selected grid points of the NOAA WAVEWATCH III® model.

3. Results of Microseism Analysis at HLG

Seismic Station HLG at Helgoland records, with interruptions, since 1903 broadband seismic data. The Geosciences Department of Kiel University operates the station incorporated in the GEOFON network of the GFZ Potsdam since 1956. Here we evaluate continuous data recorded with the STS2 broadband seismometer in the time interval 2004–2018. We obtained data of the vertical and two horizontal components of Station HLG from the GEOFON data repository (GFZ, <https://geofon.gfz-potsdam.de>, <https://doi.org/10.14470/TR560404>).

3.1. Components of Microseism at HLG

To access the temporal characteristics of the microseismic wavefield at Station HLG in the frequency domain, we calculate spectrograms for all three components of HLG from original continuous 20-Hz data. Seismic traces are corrected for the sensitivity of the STS-2 broadband seismometer and data logger. No formal restitution is performed, as further analysis is carried out in the passband of the instrument and no signal distortion expected by the recording process. Day files are read in and resampled to 5 Hz to speed up processing. To obtain the spectrograms, consecutive 30- or 120-min-long time windows dependent on the desired temporal resolution are trend removed and tapered with a cosine window of 1-min length before performing a fast Fourier transform (FFT). The absolute values of the resulting complex spectra are divided by the signal length to obtain the corresponding average amplitude spectrum. We reduce the frequency sampling by a factor of 4 by calculating the mean value of four adjacent frequencies to obtain more stable results, allowing for a better visual representation of the data and reduced memory requirements for extended study periods. The resulting frequency resolution is thus 0.0022 and 0.00056 Hz, for 30 and 120-min-long time intervals, respectively.

3.1.1. PPSD-Like Analysis

We create histograms similar to a probabilistic power spectral density (PPSD) noise analysis (McNamara & Buland, 2004) from the long-term spectrograms with 2-hr resolution (Figures S1–S3 in the supporting information) to study the amplitude distribution over the entire microseismic frequency range, the median spectral amplitude and the corresponding 10th and 90th percentiles (Figure 3). The frequency resolution of the histogram is 0.01 Hz between 0 and 2 Hz. For the calculation of the median value and the percentiles,

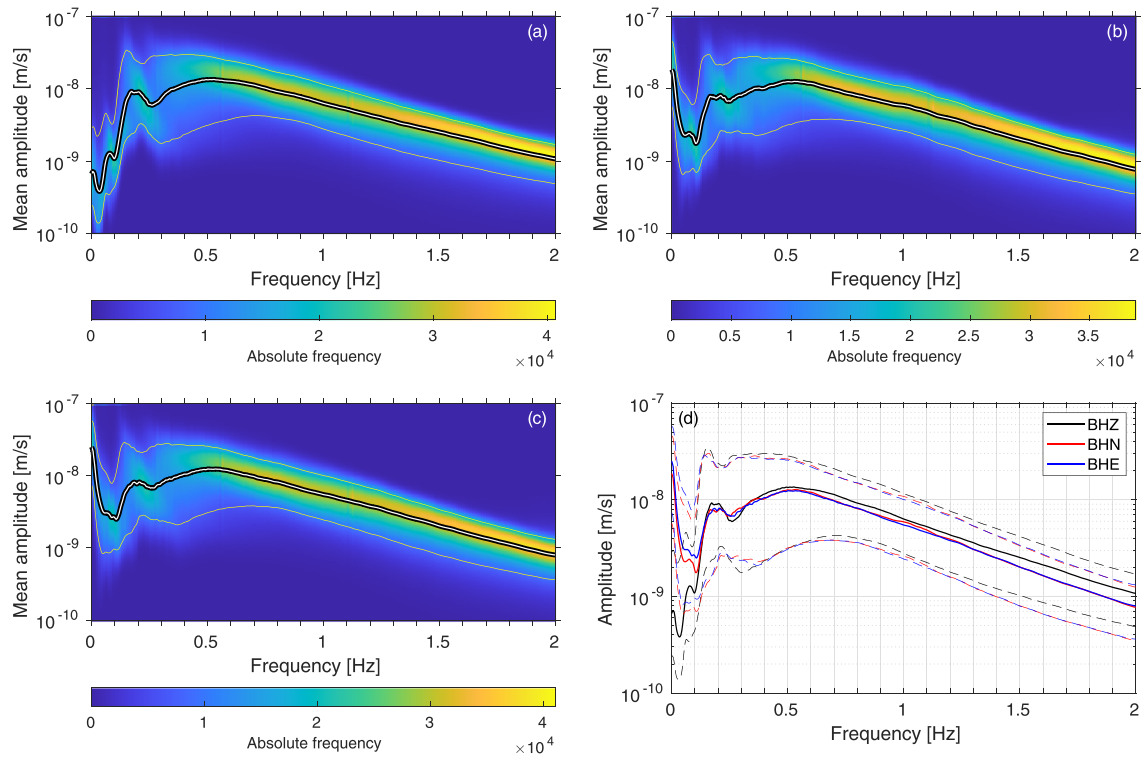


Figure 3. Histograms of mean spectral amplitudes of (a) *Z*, (b) *N*, and (c) *E* component of Station HLG on Helgoland obtained from 2-hr intervals from the period 1 January 2004 to 31 December 2018. Thick white line with black outline indicates median mean amplitude value and thin white lines the 10th and 90th percentiles, respectively. (d) Comparison of median, 10th, and 90th percentiles of the three components.

amplitude values exceeding the range between 10^{-10} and 10^{-7} m/s are not considered. We smooth median mean amplitude values with a 20-point running average. Values for the 10th and 90th percentiles are obtained by first determining the median value in a 20-point window and subsequently applying a 20-point moving averaging scheme to the resulting curve.

Results for all three components are comparable above 0.12 Hz with a pronounced peak around 0.17 Hz for the median and 90th percentile. This peak falls into the SM frequency range. Toward higher frequencies, all three curves show a pronounced and extended maximum which peaks at about 0.5 Hz. This is in the LM frequency range. The median curve in the frequency range from about 0.3–0.8 Hz shows even higher amplitudes than in the SM range. This indicates that LM dominates the average microseism wavefield at Station HLG. However, the 90th percentile in the SM range is higher than in the LM range indicating the exceptionally strong SM energy generated during infrequent but strong storm phases. At lower frequencies (below 0.12 Hz), a pronounced PM peak is only observable on the vertical component (Figures 3c and 3d). The horizontal components, on the other hand, show a higher energy level with a further sharp increase below 0.05 Hz. The corresponding global maximum toward the lower-frequency limit might be caused by tilt effects.

Figure 3 shows the average properties of the microseism wavefield at Station HLG for a time period of 15 years. Amplitudes and dominant frequencies are highly variable with time showing seasonality and dependence on the strength and motion of identified storms and the resulting sea state (see also Figures S1–S3). This effect is visible in Figures 4 and 5, which show the frequency content of the microseism wavefield during representative times in winter and summer, respectively. These time intervals were chosen for the presence of pronounced storm activity in summer/winter and a good coverage of wave height buoy data. However, they are representative for the corresponding observations during winter and summer times.

3.1.2. RPM, RSM, and LSM at HLG

In Figure 4a, we filter vertical seismic recordings at Station HLG in three different frequency bands, 0.2–1 Hz (LM frequency band, LMB), 0.08–0.2 Hz (SM frequency band, SMB), and 0.03–0.08 Hz (PM frequency band,

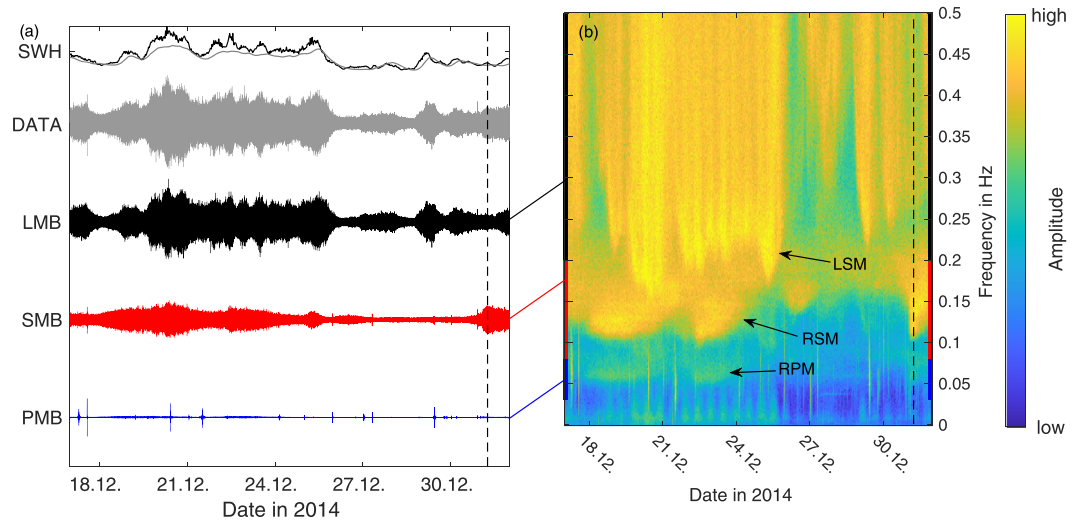


Figure 4. (a) Waveforms of SWH and filtered seismograms (vertical component) at Station HLG and (b) spectrogram of unfiltered vertical component at HLG for 15 days in December 2014. Data in (b) are displayed with a logarithmic color scale, and the frequency axis is terminated at 0.5 Hz for better visualization. Traces shown on left are as follows: SWH indicates the signal registered at a buoy near Helgoland (black) and the signal of wave heights calculated by the WAVEWATCH III® hindcast at C in Figure 1 (gray); DATA: vertical seismic component sampled at 2 Hz; LMB, SMB, and PMB: vertical component data filtered in the respective frequency bands. All seismic traces have the same axis scaling. SWH is between 1 m and nearly 6 m. Colored bars to the left and right of the spectrogram indicate the frequency ranges of the corresponding waveforms. Arrivals/wavepackages in PMB components visible in the waveforms as well as the spectrogram as high-frequency arrivals with short durations are identified with teleseismic earthquakes. Broken vertical lines in (a) and (b) indicate the same time instance that exhibits high RSM amplitudes and low SWH at Helgoland.

PMB), that roughly correspond to the globally observed frequencies of LM, SM, and PM, respectively. We will keep these frequency limits and the corresponding terminology LMB, SMB, and PMB throughout this study (see Table 1). However, this refers only to the frequency bands for analysis and does not imply a generation mechanism of the recorded ocean microseism in the respective frequency band.

LMB energy tends to correlate with SWH measured at the moored buoy HelgolandWR (HELGO in Figure 2) at a distance of less than 1 km from seismic Station HLG. SWH is defined as the mean value of the upper third of all measured wave heights in a defined time interval and provided with 30-min resolution. The temporal variability in SMB and PMB on the other hand differs strongly from the local SWH, pointing to remote sources (Figure 4a). In addition to the amplitude, also the dominant microseism frequency is modulated during a single storm event. This is visible in the spectrogram during storm activity in winter (Figure 4b).

We distinguish three different signal bands in Figure 4b: (a) A high-amplitude signal in the range 0.2–0.5 Hz, showing a variation in strength and dominant frequency in sync with the local SWH. Lower frequencies are observed during times with higher wave heights as observed by Webb (1998). We thus associate this signal, often called SPSM in former studies, with LSM. (b) A high-amplitude signal in the frequency band 0.1–0.2 Hz that shows a smoother variation with time than the LSM signal and a significantly weaker correlation with the local wave height. Notice, for example, the high amplitude signal in the spectrogram around 0.15 Hz toward the end of the depicted period—indicated by the broken vertical line—which shows no correspondence in the wave height data at left. We suggest a remote origin of these signals and thus term them RSM. (c) A weaker signal with half the frequency of RSM and comparable temporal behavior. We identify this signal as RPM.

The separation between LSM and RSM by means of frequency, however, is not sharp as can be seen in the spectrogram. A fixed, time-invariant frequency limit between LSM and RSM will lead to a wrong attribution during some time intervals.

3.1.3. Identification of LPM at HLG

The strong correlation between the spectral energy of the LSM above 0.2 Hz and the locally recorded SWH is season independent (Figures 5a and 5c). The LSM dominates the spectrogram during summer. Figure 5c

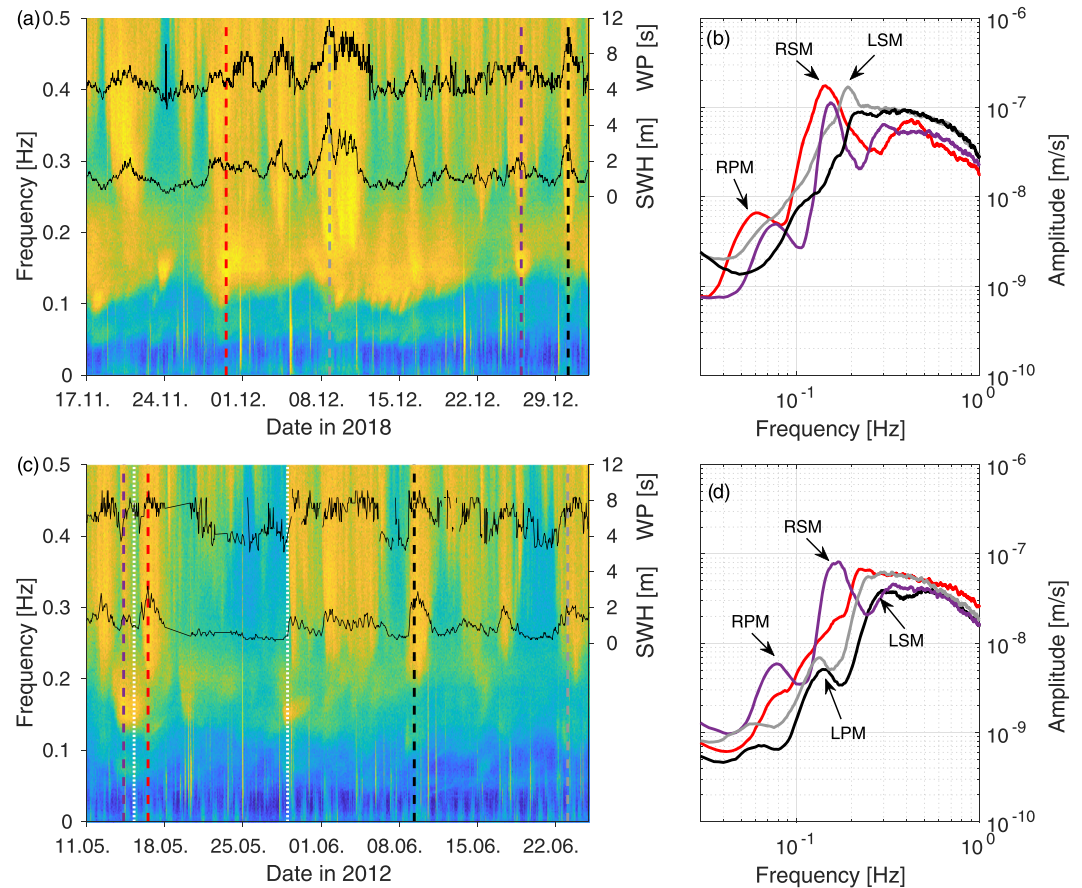


Figure 5. (a and c) Z component spectrograms for a 45-day interval in winter and summer, respectively. Same color scale as in Figure 4b. Vertical broken lines indicate time intervals for which the time-averaged spectra are shown in (b) and (d), respectively. Black lines indicate SWH and dominant wave period (WP) measured at wave buoy HelgolandWR. (b and d) Time-averaged amplitude spectra of four distinct time intervals consisting of seven consecutive 30-min time intervals each. Colors identify the different time instances marked in the spectrograms. Time-averaged spectra smoothed with a 10-point running average. Expressions of RPM, RSM, LPM, and LSM in the spectra indicated by black arrows.

indicates that ocean wave periods recorded close to Helgoland generally correlate well with the lowest LSM frequencies (see, e.g., 8–11 June 2012 with LSM frequencies down to 0.2 Hz and dominant ocean wave frequency at Helgoland close to 0.1 Hz), being roughly double the ocean wave frequency. The correlation between SWH at Helgoland and RSM registered at HLG at frequencies below 0.2 Hz in summer is even weaker than during winter. High amplitudes below 0.2 Hz do not necessarily correlate with high sea states at Helgoland (e.g., 15 May 2012 and 29 May 2012 in Figure 5c; marked by dotted white lines) while many sea states with wave heights around 2 m do not show energy in the typical SM frequency range around 0.15 Hz. A possible interpretation of this observation is the fact that periods of ocean waves at Helgoland are generally significantly lower than 14 s (Figures 5a and 5c).

The RPM identified in Figure 4b is hard to see in the spectrogram during summer but can be identified during periods of strong RSM (14 May 2012 in Figure 5c; lilac broken line). However, during times of strong LSM and a simultaneous absence of RSM energy (e.g., 9 June 2012 or 22 June 2012 in Figure 5c; broken black and gray lines, respectively), a second, weaker peak is observable slightly above 0.1 Hz in the spectrogram. That means during summer, two peaks above 0.1 Hz and above 0.2 Hz, respectively, are visible at the same time. As the lower-frequency peak is at half the frequency of the LSM and thus of comparable frequency as the locally observed ocean waves, we associate it with LPM. The observations suggest that LSM and LPM are generated locally within the German Bight and RSM and RPM at more distant sources in the North Atlantic.

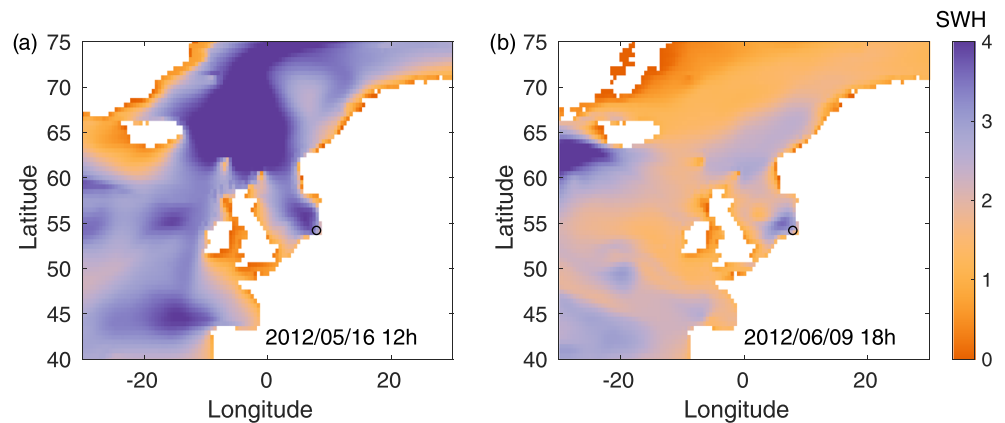


Figure 6. Significant wave height as obtained from WAVEWATCH III® model for (a) 16 May 2012, 12 hr, and (b) 9 June 2012, 18 hr.

During winter (Figure 4b), the LSM/LPM pattern is not so easily discernible. The higher-frequency LSM peaks are generally shifted to lower frequencies (partly below 0.2 Hz, Figure 4b), and a corresponding LPM peak at half that frequency is difficult to see due to the higher RSM energy in winter caused by extensive and numerous storm systems in the North Atlantic.

The presence of LPM during summer is getting more visible when looking at the respective amplitude spectra. Figure 5 shows in addition to the corresponding spectrograms the time-averaged amplitude spectra for selected time intervals in summer and winter, respectively. In summer, beside the dominant LSM energy in the frequency range above 0.2 Hz, another local maximum at half the dominant frequency is visible around 0.15 Hz (black and gray curves in Figure 5d). We interpret this second maximum as the expression of LPM. During winter, however, the spectral energy is monotonously decreasing toward frequencies significantly below 0.1 Hz for times with high energy around 0.2 Hz (or slightly below, gray and black lines in Figure 5b). This is due to the generally higher background energy level below 0.2 Hz during winter caused by storm activity in the North Atlantic. This behavior can also occur during summer in case of synchronous local and remote storm activity (red line in Figure 5d). For time instances with strong energy in the 0.15-Hz range (the typical SM range) and low to modest energy above 0.2 Hz, there is a clear local maximum between 0.05 and 0.1 Hz for both summer and winter times (red and lilac curves in Figure 5b and lilac curve in Figure 5d). During these time intervals, we observe RSM and RPM from distant sources in the North Atlantic. The general energy level is higher during boreal winter over the displayed frequency range from 0.03–1 Hz, as visible in Figures 5b and 5d.

Results are comparable for the horizontal components. This can also be seen in the spectrograms of all three components spanning the entire study interval (Figures S1–S3) where a clear annual periodicity is recognizable.

3.2. Sources of RSM and LSM Recorded at HLG

Figure 6 presents the SeaWaveHeights generated by the NOAA WAVEWATCH III® model for two reference instances in summer 2012 (as in Figures 5c and 5d and discussed before). For 13 May 2012, 12 hr (red lines in Figures 5c and 5d) the WAVEWATCH III® modeling predicts SWHs in the main part of the North Atlantic and the North Sea (Figure 6a). The measured SWHs at Helgoland are in agreement with the model (Figure 5c). It is not possible to identify LPM signal in the specific case due to the strong RSM overlapping the LPM frequency band. On the 9 June 2012, 18 hr (black lines in Figures 5c and 5d) we observe significant wave activity around Helgoland in the German Bight and much less in the North Atlantic (Figure 6b). The LPM signal can be seen in Figure 5d (black line) as a secondary maximum at 0.15 Hz, and it is in good agreement with the observed dominant ocean wave period recorded by the buoy at Helgoland at the same time (Figure 5c). This consistency supports the identification of this signal component as LPM. These observations support the hypothesis of sources of LM located within the German Bight, while remote microseism originates in the North Atlantic.

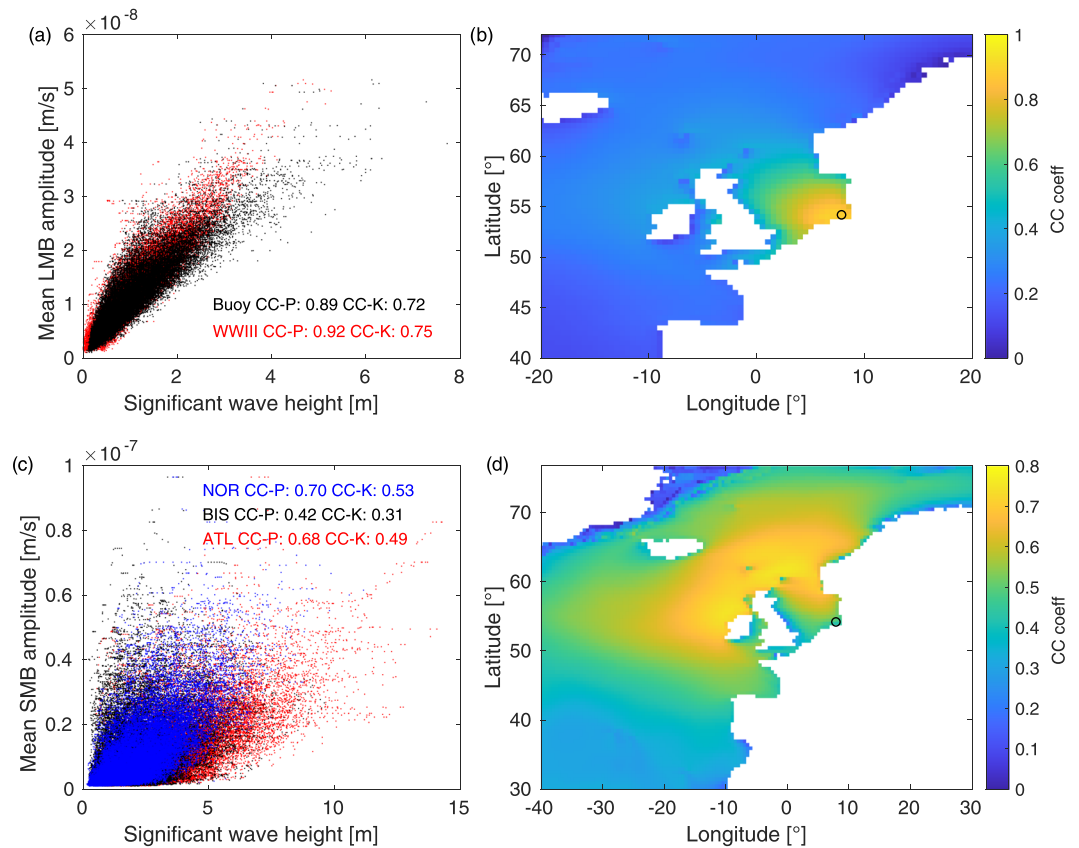


Figure 7. (a) Correlation between the mean LMB amplitude and the modeled significant wave height at grid node 54.0°N/8.0°E of the WAVEWATCH III® model (red) and at the buoy close to Helgoland (black) in the time interval 1 February 2005 to 31 December 2014. (b) Spatially resolved correlation coefficient (CC-P) between the WAVEWATCH III® output and the mean LMB amplitude for the time interval 1 January 2012 to 31 December 2014. (c) Correlation between the mean SMB amplitude and the modeled significant wave height at three grid nodes of the WAVEWATCH III® model (NOR—Point A, BIS—Point D, and ATL—Point B in Figure 1, respectively) in the time interval 1 February 2005 to 31 December 2014. (d) Spatially resolved correlation coefficient (CC-P) between the WAVEWATCH III® output and the mean SMB amplitude for the time interval 1 January 2012 to 31 December 2014. Circles in (b) and (d) indicate the location of Helgoland.

We perform a correlation analysis between SWH from buoy data and the closest grid point of the WAVEWATCH III® model (WWP1 in Figure 2) with mean LMB amplitudes (Figure 7a) to support our qualitative evaluation. The strong correlation between mean LMB amplitude and SWH for buoy and model data can be seen in Figure 7a. CC-P and CC-K refer to the Pearson and Kendall correlation coefficients, respectively. While CC-P is the well-known sample correlation coefficient and tests for a linear correlation between two variables X and Y , the so-called Kendall's tau (Kendall, 1970) does not assume a linear correlation and is robust against outliers. It is calculated by the formula $\tau_b = (C - D) / [(C + D + T_x) * (C + D + T_y)]^{-1/2}$, where C and D are the number of concordant (i.e., $x_i > x_k$ and $y_i > y_k$) and discordant ($x_i > x_k$ and $y_i < y_k$) pairs of SWH and mean LMB amplitude time series, respectively. T_x and T_y are the number of equal variable pairs ($x_i = x_k$) or ($y_i = y_k$) in the time series \mathbf{x} and \mathbf{y} (see Juretzek & Hadziioannou, 2017).

We obtain correlation coefficients of 0.8 for the region of the German Bight and a quick decrease toward the northern North Sea and the North Atlantic (Figure 7b). This indicates that sources of LMB energy, expected to be dominated by LSM, are mainly confined to the German Bight around HLG.

Similarly, a dominant source in the Northern Atlantic is revealed by correlation between the modeled wave data and the mean SMB amplitudes (Figure 7d). Sources close to Norway and Ireland show similar correlation coefficients with on average higher SWH in the Atlantic west of Ireland while the Gulf of

Biscay exhibits correlation coefficients comparable to the North Sea (Figure 7c). The relatively low correlation coefficient for the region around Helgoland, indicates that the dominant source region of the LMB energy (Figure 7b) does not significantly contribute to the microseism wavefield in the SMB. Furthermore, this indicates that there is only a weak to moderate correlation between the sea state around Helgoland and in the North Atlantic. The lower maximum values of the correlation coefficient for SMB energy than for LMB energy can be explained by the multitude of SMB sources in the North Atlantic while only the immediate surrounding of Helgoland seems to be relevant for the generation of LMB energy.

3.3. LMB and SMB H/V Ratios

Due to its generation mechanism, PM in general exhibits a Love-to-Rayleigh wave ratio higher than SM, which mainly creates Rayleigh waves (Juretzek & Hadziioannou, 2016). We calculate horizontal-to-vertical (H/V) ratio as a proxy for the ratio of Love-to-Rayleigh amplitude. We perform a spectral division of total horizontal and vertical spectrograms to obtain H/V ratios as a function of time and frequency. In addition, we also divide the mean horizontal amplitude in the SMB and LMB ranges based on 2-hr time signal windows by the respective vertical values. Mean amplitudes are calculated from the spectra of the 2-hr time windows making up the spectrograms of Figures S1–S3. First, we apply a 20-point running average to each spectrum. Afterward, we extract the mean value of the squared amplitude spectrum in the respective frequency band and take the square root. Finally, we perform a median filtering on the resulting SMB time series with a 5-point moving window to remove the possible influence of teleseismic events on the SMB. For the LMB, no median filtering is performed due to the minor influence of teleseismic events in this frequency range. The vector sum of the two horizontal components is calculated before it is divided by the vertical value. We remove nondefined values due to missing data as well as outliers by linear interpolation using adjacent values. For the SMB an outlier was defined, when the H/V value was outside the range 0.6–4 and for LMB when it was outside the range 1–2. These values were determined by visual inspection of the H/V time series before outlier removal. Outliers resulted mainly from spurious signals on one of the components not completely removed during the previous median filtering or edge effects. Missing data and outliers constitute only about 0.5% of the total H/V data in the SMB and LMB.

3.3.1. H/V Value Statistics

The median H/V value of the SMB and LMB for the whole study period is comparable (Figure S4a and S4b) at about 1.3, while their distribution functions exhibit considerable differences. SMB H/V values have a rather symmetric distribution around the mean value (Figure S4a), while the distribution of the LMB H/V values exhibits a considerably higher positive skewness (7.5 vs. 1.6) indicating a more pronounced tail for values above the mean. Splitting up the H/V ratios of the SMB into two time intervals from May–September (Figure S4c) and October–April (Figure S4d) indicates a higher variability during summer times than winter times (standard deviation of 0.3 vs. 0.14 although the median/mean values and the skewness of the distributions are comparable). The reason for this variability can be investigated by studying the behavior during summer in detail.

3.3.2. Temporal Variability of H/V Values

Figure 8a displays the result of spectral division for 2 months in summer 2012. We can observe a considerable variability of the H/V value in the different frequencies within the band shown in Figure 8a. During times of significant local wave activity, we observe periods with increased H/V ratios in the frequency range 0.11–0.2 Hz and at the same time lower H/V ratios above about 0.25 Hz in the LMB (e.g., 9 June 2012, indicated by broken black line). This suggests that LPM, which we identified in Figures 5c and 5d in this time interval, causes these higher than average H/V values of about 3. The elevated H/V values of LPM show a periodic pattern in the semidiurnal range (e.g., around the broken black line in Figure 8a) reminiscent of the patterns observed in the spectrograms in Figures 4b, 5a, and 5c for the mean LMB amplitudes above about 0.2 Hz (e.g., between 19 and 26 December 2012 in Figure 4b).

In addition, time intervals with increased local wave activity and a simultaneous absence of increased H/V values in the frequency range between 0.1 and 0.2 Hz are observed (e.g., 16 May 2012, indicated by broken red line in Figure 8a). The dominant influence of RSM (see also Figure 6a) during these times overshadows the effect of LPM.

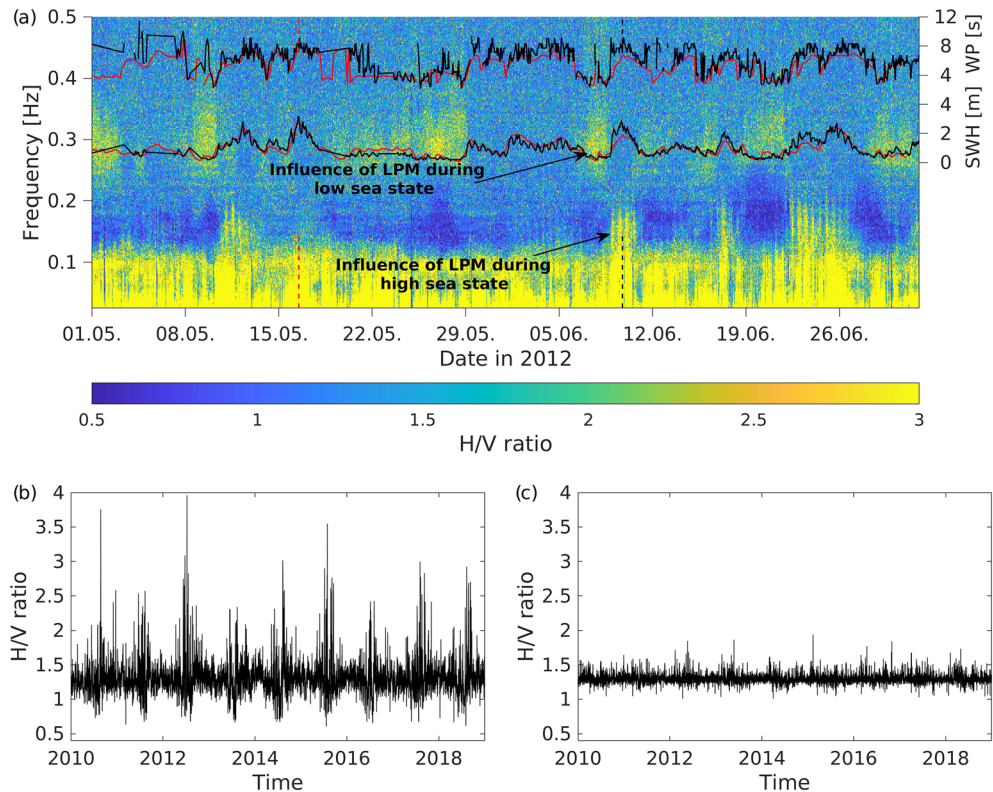


Figure 8. (a) H/V ratio obtained from the respective amplitude spectra (Figure 5c and corresponding horizontal spectrograms) by spectral division for two months in summer of 2012. Black and red lines indicate SWH and wave period (WP) obtained from buoy HelgolandWR and the nearest WAVEWATCH III® grid point (WWP1 in Figure 2), respectively. Red and black vertical broken lines indicate the same time instances as in Figures 5c and 5d. (b and c) H/V ratio in the SMB and LMB, respectively. For better visibility only the years 2010–2018 are displayed.

Furthermore, time intervals with exceptionally low H/V values below one in the SMB and simultaneously elevated H/V ratios in the LMB are observed during quiet local sea states. This is seen, for example, on the 8 May and the 8 and 20 June 2012 (Figure 8a). The higher H/V values above 0.2 Hz can be explained by a shift of LPM into this frequency range as suggested by dominant ocean wave periods below 4 s during these times. During winter, no significant correlation between the H/V value in the SMB and the local SWH can be observed (Figures S5a and S6a). The generally higher RSM energy during winter overpowers the LPM influence on the H/V value. These observations hold in general for all investigated years and indicate a considerable Love wave contribution to the LPM wavefield.

Studying H/V values in the SMB and LMB over the entire study period supports the observations gained from shorter times. The H/V ratio in the SMB shows a strong variability during summer months and a rather constant value of about 1.3 during winter months (Figure 8b). This variability during summer can be seen in all investigated years (Figures 8a, 8b, S5b, and S6b) with high H/V values corresponding to a dominant influence of LPM. The H/V ratio in the LMB (Figure 8c) is rather constant around 1.3 indicating a stable generation mechanism at local sources in the German Bight. The same average H/V value in the LMB (Figure 8c) and the SMB during winter (Figure 8b) suggests comparable Love-to-Rayleigh wave ratios for LSM and RSM.

3.3.3. Correlation Between SMB H/V Ratio and Local Wave Height

Because local wave activity around Station HLG and the resulting LPM have a higher influence on the H/V ratio in the SMB during summer due to the frequent absence of RSM energy from the North Atlantic, we expect a higher correlation between local sea state and SMB H/V ratio during summer. We see this in Figure S7, which plots the H/V ratio of the SMB over SWH separately for each month. Additionally, the Pearson and Kendall correlation coefficients are calculated for each month separately and given in the upper right corner of each subplot.

For May–September, the Pearson correlation coefficient is larger than 0.5, indicating a positive correlation between SWH and H/V ratio in these time intervals. During the rest of the year, the correlation coefficients (both Pearson and Kendall) are below 0.5 indicating only a weak or no correlation between the variables. Except for January, the absolute value of the Pearson coefficient is always higher than that of Kendall's coefficient.

Observations of the buoy are in general agreement with hindcasts from the WAVEWATCH III® model for the nearest grid point (54°N/8°E), and thus, the longer time interval (1 February 2005 to 31 December 2018) available from the hindcasts can also be used to obtain reliable results for time periods without buoy data (Figure S7). These results support the earlier conclusions in a quantitative way.

4. Tidal Modulation of Microseism at HLG

In the spectrograms, we can track seasonal variations (Figures S1–S3), variations with single storm systems and higher-frequency modulations (Figures 4b, 5a, and 5c) of the seismic energy and the dominant frequency. In addition, the SMB H/V ratio shows some pronounced higher-frequency modulations mainly during summer months (Figure 8a).

4.1. Tidal Signals in Microseism at HLG

To study the possible periodicities in the microseism energy budget and H/V ratio in a more quantitative manner and to compare them with the dominant frequencies present in possible driving forces (wave height, water level, and air pressure), we calculate the Fourier spectra of frequency-averaged mean amplitude profiles. We again use the time series of mean SMB and LMB amplitudes utilized previously for the calculation of the H/V ratios in Figures 8b and 8c. In addition, we also use the mean amplitudes in the PMB. The time series of mean amplitudes with 2-hr resolution for each frequency band are trend removed, transformed into the frequency domain via standard FFT, normalized, and displayed in Figure 9 for the BHZ component of HLG. Apart from a dominant annual periodicity (Figure 9a) present in all frequency bands, we find peaks in the amplitude spectrum of the mean LMB amplitudes with diurnal, semidiurnal and quarter-diurnal cycles. They are not present in the PMB and SMB results.

In analogy to the spectra of the mean amplitude time profiles in Figure 9, we calculate spectra of the H/V ratios in SMB and LMB presented in Figures 8b and 8c, to identify possible periodic phenomena. Normalized H/V spectra of SMB and LMB are calculated analogous to the spectra of mean amplitudes and displayed in Figure 10. Absolute values of these spectra are small with a maximum value of about 0.035 (H/V)/Hz for SMB and a factor of 3 smaller for LMB. Like for the mean amplitudes there is a peak at a period of 1 year indicating some annual variability. Interestingly, there are distinct peaks in the diurnal and semidiurnal period range found for both SMB and LMB. The strong semidiurnal H/V SMB peak (Figure 10; the corresponding H/V variability is visible, e.g., in the H/V ratio at 0.1–0.2 Hz for time periods 10–11 June 2012 and 22–26 June 2012 in Figure 8a) allows the determination of the phase relationship with respect to water level and wave activity, which shows the same frequency peaks.

4.2. Tidal Signals in Sea Level, SWH, and Air Pressure

To identify possible correlations of these peaks with peaks contained in spectra of environmental parameter time series near Station HLG, we compare the LMB spectrum to spectra of sea level, air pressure, and SWH. We obtain spectra with identical frequency resolution for the period 1 January 2004 to 31 December 2018 by resampling all available time series (microseism, sea level, air pressure, and SWH) to a sample rate of one sample per hour.

Water level data are obtained from the NWS data portal for the Helgoland harbor gauge station. Apart from the diurnal, semidiurnal, and quarter-diurnal peaks present in Figures 11a–11c, also a peak at a period of 1 year is present in the water level data, indicating the seasonal influence on tides in the North Sea. The most prominent peak at a period of 12 hr 25 min is the so-called M2 partial tide caused by the rotation of the Earth and the concurrent motion of the Moon. The lunar day is about 24 hr 50 min, and in this time frame two ocean tide peaks pass each point at the Earth surface. The second highest peak for the ocean tides, S2 partial tide (12hr0m), is controlled by the time for two consecutive meridian transits of the Sun (solar day). For Helgoland, as for the North Atlantic and neighboring areas, diurnal partial tides (e.g., K1, O1, a combination of the frequencies of the lunar day, and the tropical month) are significantly smaller than semidiurnal tides.

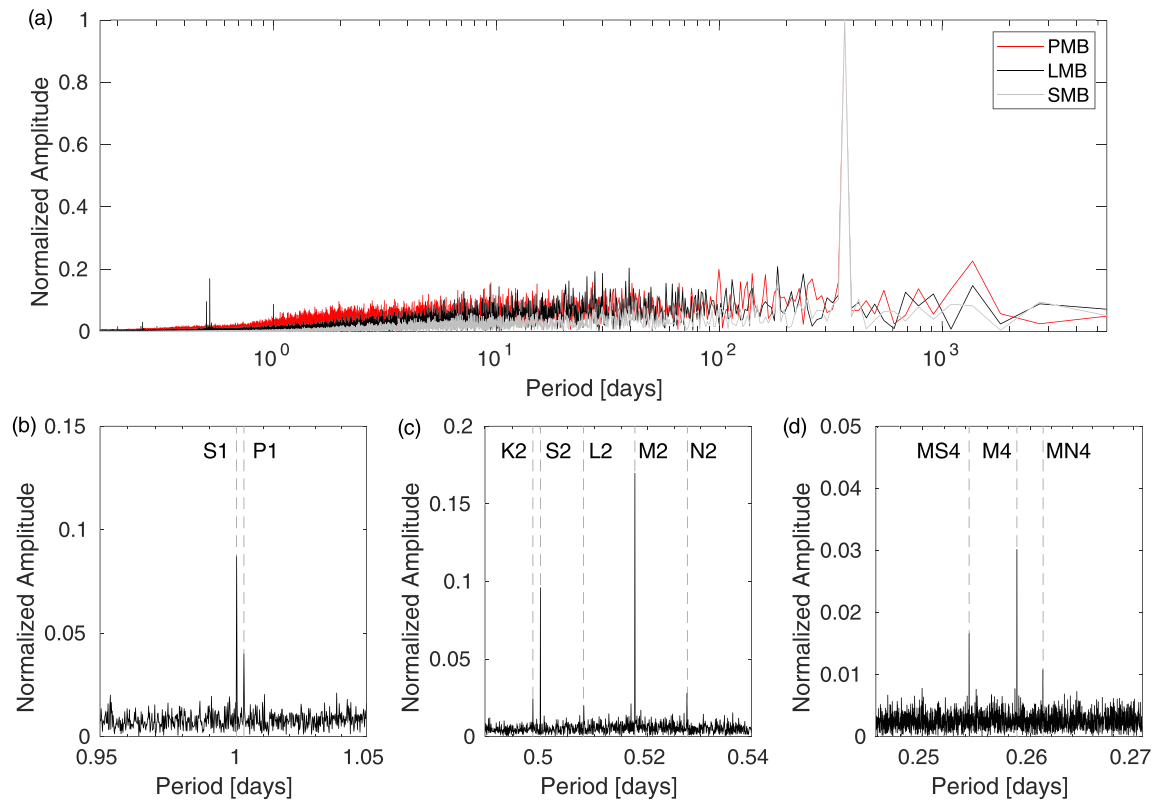


Figure 9. (a) Normalized spectra of mean amplitude profiles over the study period for PMB, SMB, and LMB. (b–d) Zoom of the LMB data from (a) in the diurnal, semidiurnal, and quarter-diurnal frequency ranges, respectively. Broken vertical lines and corresponding labels indicate partial ocean tides in the respective frequency ranges. Waveform data are from BHZ component of HLG.

On the other hand, a significant number of pronounced quarter-diurnal tidal peaks (MS4, M4, and MN4; Figure 11c) is also visible in the LMB data (Figure 9d).

We calculate the amplitude spectrum of SWH at Helgoland from the data of buoy HelgolandWR and find pronounced peaks at M2, S2, and M4 (Figures 11e and 11f) but no peak in the diurnal frequency range (Figure 11d). This indicates that apart from storm systems also the ocean tides and the corresponding ebb and flood currents modify the observed ocean wave field around Helgoland. The fact that the amplitudes of the semidiurnal and quarter-diurnal peaks in the spectra of SWH are of the same order of magnitude indicates that the SWH is also influenced by the asymmetry of the ocean tidal signal that gives rise to the quarter diurnal peaks in Figure 11c. Because we observe semidiurnal and quarter-diurnal peaks in the ocean wave spectrum at the frequency of peaks in the spectrum of the LMB, the tide-modulated ocean wave state might

cause the modulation with ocean tidal periods observed for the microseism energy in the LMB as also observed by Beucler et al. (2015) for the French Atlantic coast.

Air pressure data are provided by Deutscher Wetterdienst (DWD) for Station ID 02115 at Helgoland with a temporal resolution of 1 hr. The corresponding amplitude spectrum in Figures 11g–11i displays peaks with diurnal (S1) and semidiurnal (S2) periods and several shorter-period contributions in the quarter-diurnal range not associated with ocean tidal periods. While the semidiurnal frequency is also present in the spectrum of the water level and the SWH, the exact diurnal peak that is found in the LMB microseism amplitude is not so easily recognizable in the other two spectra. This might indicate some connection between the air pressure and the microseism energy in the LMB.

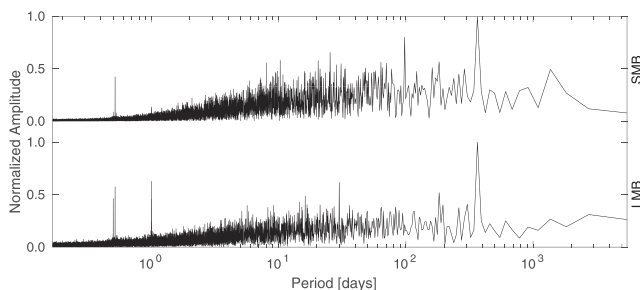


Figure 10. Normalized spectra of the H/V time profiles of the LMB and SMB frequency bands.

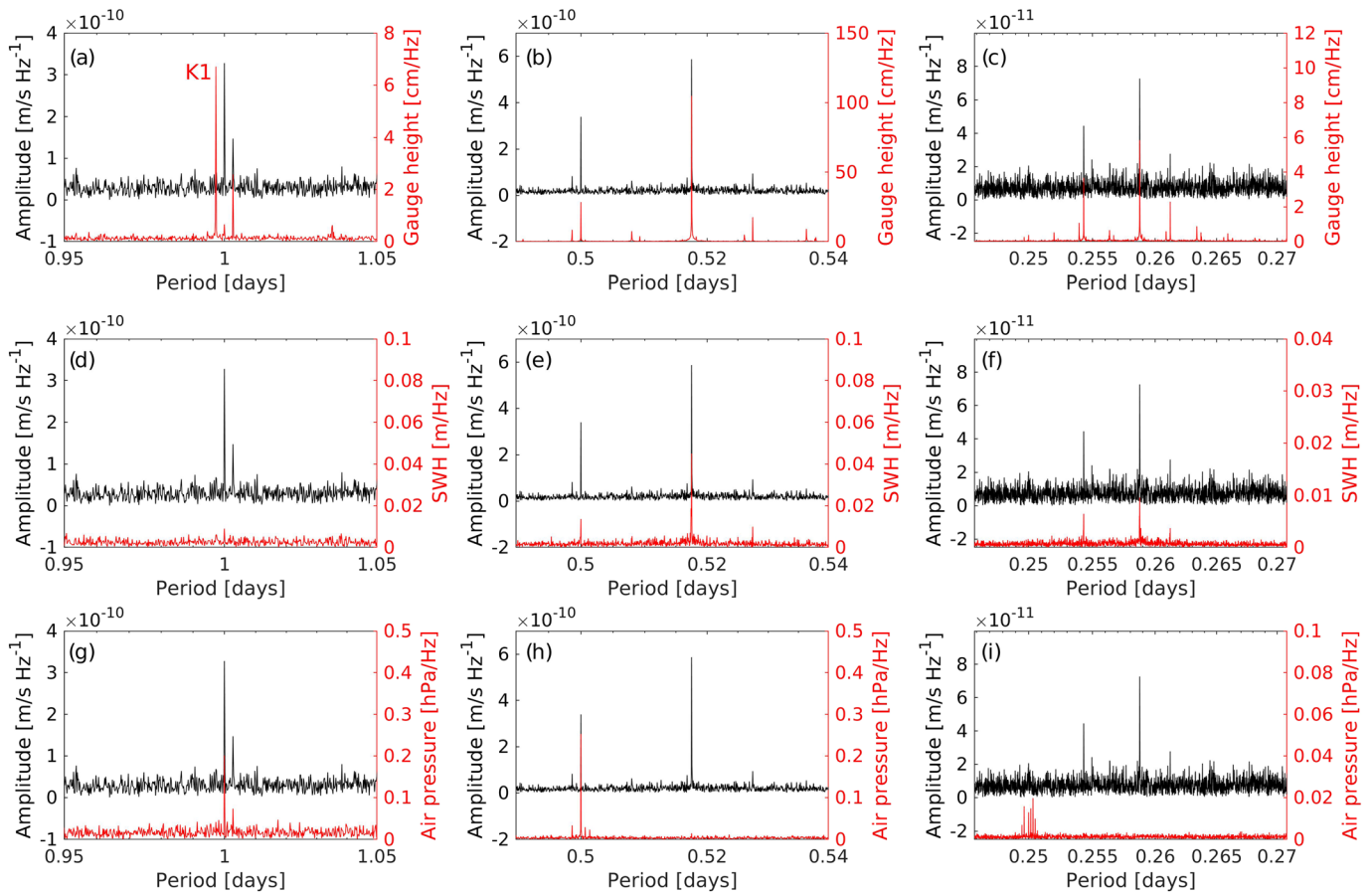


Figure 11. Amplitude spectra of water level (a–c), significant wave height (d–f) and air pressure (g–i) in the diurnal, semidiurnal, and quarter-diurnal period range (red curves). Black curves show the spectrum of the vertical component of the LMB from Figure 9a. All spectra calculated for the whole study period with 1-hr sampling.

4.3. Phase Relation of Microseism Energy, H/V Ratio, Water Level, and Wave Height

To investigate the phase delay and thus possible causative relationships between the dominant semidiurnal signal observable in the seismic data, the water level and the SWH, we perform a temporal correlation analysis between these time series. Figure 12a shows the time series of the mean vertical component LMB amplitude, SWH, and water level, that is, gauge data at station Helgoland, and its first time derivative for a time period of 18 days in summer 2012 also covered in Figures 5c and 8a. Time series are resampled to a common sampling interval of 30 min, and time series of mean amplitude and SWH are slightly smoothed with a 3-point moving average. We normalize water level data to obtain values between 0 and 1. All other curves are divided by their maximum absolute value in this interval. The general shape of the curves of mean LMB amplitude and SWH fits well but the higher-frequency modulations are more complicated. During many tidal cycles, the maximum of the mean LMB amplitude precedes the maximum water level height. The asymmetry in the time derivative of the water level with larger positive than negative values indicates different strengths of the currents during rising and falling tide with higher values during rising tide.

From the correlation functions in Figure 12b we cannot distinguish any time lag between the maximum water level and maximum SWH. The maximum in mean LMB amplitude is 2.5 hr earlier than the water level maximum and the maximum in the H/V ratio in SMB is 1.5 hr earlier than it. The temporal variability in the SMB H/V ratio is mainly caused by high H/V values of LPM during times when LPM dominates this frequency range (Figure 8a). The semidiurnal modulation of the H/V ratio in this frequency band is apparent from Figure 10. Thus, a correlation of the mean LMB amplitude and the SMB H/V ratio with the water level can be used to obtain the phase shift between LSM and LPM with respect to the water level maximum,

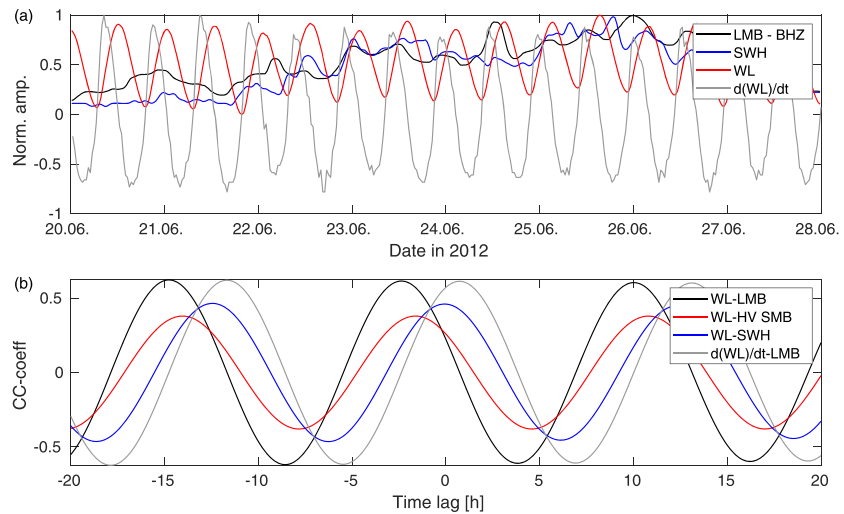


Figure 12. (a) Normalized time series of mean vertical component LMB amplitude (LMB-BHZ), SWH, water level according to gauge data (WL), and time derivative of water level, that is, water level change ($d(WL)/dt$). See text for details of normalization. (b) Correlation functions between water level and mean LMB amplitude, H/V ratio of SMB and SWH, respectively, and time derivative of water level and mean LMB amplitude. Correlation was performed for the 1-year interval from 1 July 2011 to 1 July 2012 on time series with 30-min sampling, filtered between 8 and 16 hr.

respectively. The time shift between the maximum rate of water level change ($d(WL)/dt$) and the maximum mean LMB amplitude is about 40 min with the microseism maximum trailing the maximum in water level change. Performing these calculations for other 1-year periods or longer ones leads to comparable results.

These results show that the energy maxima of LSM and LPM precede both the local water level maximum and the maximum in SWH, while water level and SWH show no time shift relative to each other.

5. Narrowing Down the LSM Source Regions

Results of the correlation analysis are compatible with LSM and LPM sources to the west of Helgoland. The maximum of the tidal signal at a gauge station close to wave buoy RZGN1 at the border between Germany and the Netherlands (Figure 2) is about 1 hr earlier than the maximum at Helgoland. A time shift of 1.5 hr between the SMB H/V ratio (i.e., the dominant LPM signal) and the water level signal (Figure 12b) would thus indicate a source off the coast of the Netherlands for LPM. The time shift of 2.5 hr between LSM and the water level (Figure 12b) would indicate a source even further to the west. This is valid under the assumption that the maximum microseism energy is produced during the water level maximum, as suggested by former studies (Beucler et al., 2015; Okihiro & Guza, 1995).

To address the question of possible source regions of LSM in the German Bight and the North Sea, we also investigate the mean LMB amplitude, the sea level and the SWH at stations in the surrounding of Helgoland (see Figure 2 for station locations). Seismic Station G021 at the Netherland coast of the North Sea is at 50-m depth in a borehole, equipped with three 4.5-Hz geophones and part of the Netherlands Seismic and Acoustic Network. We restituted data of this station using its transfer function. Stations IGAD, SKMB, BSEG, and KUDEN are broadband stations belonging to the German Regional Seismic Network and are only corrected for instrument sensitivity.

While Station G021 is less than 1 km from the coastline, Stations KUDEN, IGAD, and SKMB are at distances of approximately 15, 30, and 38 km to the nearest North Sea coastline, respectively. SKMB is closer to the Baltic Sea than to the North Sea (Figure 2). BSEG is at a distance of about 90 km to the closest North Sea coastline.

G021 exhibits a similar behavior in the semidiurnal period range of the amplitude spectrum as Station HLG. Distinct peaks at M2 and S2 are observable (Figure 13a). IGAD, SKMB, and KUDEN also show the M2 peak

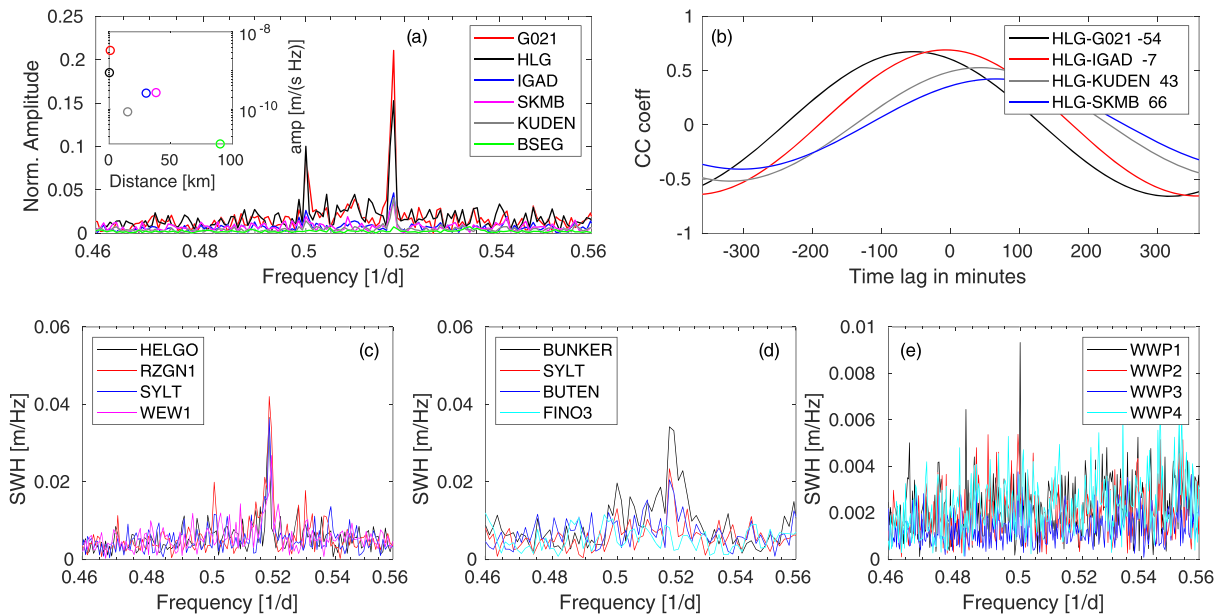


Figure 13. (a) Normalized amplitude spectra of mean vertical component LMB amplitude with hourly resolution for time interval 1 July 2018 to 1 July 2019 for stations shown in Figure 2. Inset shows the absolute value of the amplitude spectrum at the frequency point closest to M2 over the distance of the station to the closest North Sea shoreline. Color coding of circles corresponds to stations given in the legend of (a). (b) Cross-correlation functions and corresponding time lags of its maxima of mean vertical component LMB time series used to create amplitude spectra in (a). (c) Amplitude spectra of significant wave height measured in time interval 31 December 2017 to 31 December 2018 at moored buoys in the North Sea. (d) Amplitude spectra of significant wave height measured in time interval 1 March 2019 to 3 August 2019 at moored buoys in the North Sea offshore the island of Sylt. (e) Amplitude spectra of significant wave height as calculated with the NOAA WAVEWATCH III® model for the 2-year interval 1 January 2017 to 31 December 2018. Locations of buoys and grid points presented in (c)–(e) can be found in Figure 2.

but with smaller amplitude. We observe a clear decrease of the amplitude with increasing distance from the coastline (see also inset in Figure 13a). At BSEG, no M2 amplitude peak is discernable.

The decrease in the energy of the LSM signal with distance is also visible in the station spectrograms (Figure S8). HLG and G021 show significant energy up to a frequency of 1 Hz, while SKMB is significantly depleted in energy above 0.5 Hz and BSEG shows no energy in the LMB. The recorded RSM in the SMB on the other hand is very similar at HLG, SKMB, and BSEG. At G021, lower frequencies are considerably compromised due to the missing sensitivity of the geophone with a corner frequency of 4.5 Hz. This amplitude decrease with distance suggests that the LSM sources are close to the nearest North Sea shoreline. Thus, a source of LSM energy more than 100 km away from HLG, situated offshore the coast of the Netherlands, as compatible with the time shift between the ocean tidal maximum and the maximum of the mean LMB amplitude (Figure 12b), seems unlikely. This implies that the maximum of the LSM energy subjected to tidal modulations is not in sync with the local SWH maximum.

Similar to Figure 12b we also cross-correlate 1-year-long time intervals of mean LMB amplitude filtered between 8 and 16 hr with clearly discernable M2 peaks (i.e., Stations HLG, G021, SKMB, and KUDEN) to obtain the time shift of the LMB amplitude maxima. This energy at G021 and IGAD peaks 54 and 7 min before it peaks on Helgoland, respectively (Figure 13b). To gain the necessary temporal resolution, time series are spline interpolated to a 1-min sampling interval. For KUDEN and SKMB, we observe the peak energy 43 and 66 min later than at HLG, respectively (Figure 13b). These time delays are in agreement with the delay in ocean tide maxima observed at tide gauge station at the offshore side of the Wadden Sea islands (Figure 14). At the coastline, tidal maxima arrive later due to the shallow bathymetry and effects caused by the islands (Figure 14).

While several wave buoy stations along the North Sea coast observe a clear M2 frequency peak (Figure 13c), the amplitude seems to decrease with increasing distance from the coastline (Figure 13d). For station FINO3, located approximately 70 km from the closest coastline (Figure 2), no M2 peak is observable in

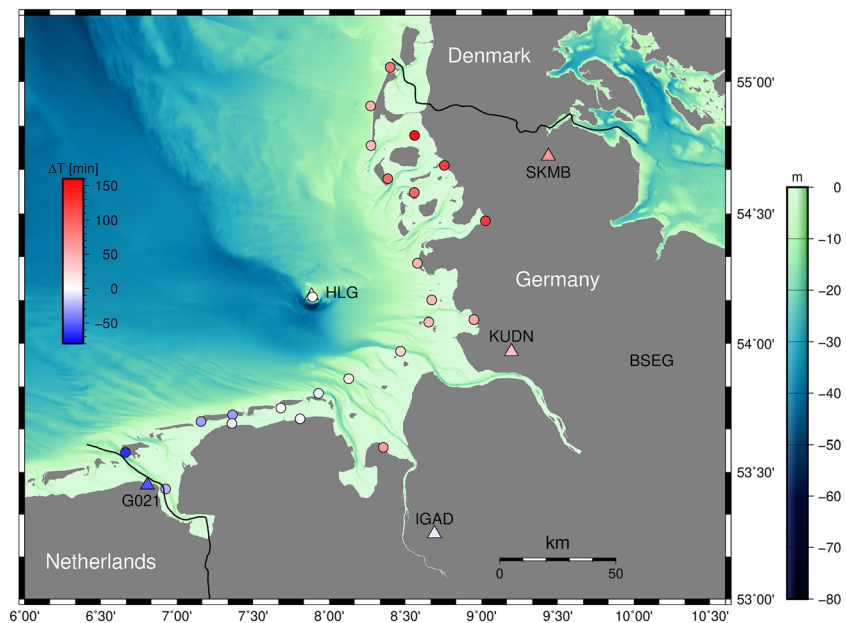


Figure 14. Time lag between water level maximum and maximum in mean vertical LMB amplitude between Helgoland and surrounding gauge stations (dots) and seismic stations (triangles), respectively. Color coding of symbols indicates time offset relative to Helgoland gauge station and seismic Station HLG, respectively, in minutes. Negative values indicate earlier maxima relative to Helgoland and positive later, respectively.

the data during the investigated interval. Stations closer to the coastline (BUTEN and SYLT) show this peak, which is strongest close to the shore (BUNKER is at a distance of less than 500 m to the coastline of the island of Sylt).

In the WAVEWATCH III® model we observe no semidiurnal M2 peaks. This was already an outcome of the time plots of observed and modeled SWH in Figure 8a, where the oscillation of the SWH with the tidal signal after 29 May 2012 is visible in the buoy data (black line) and not in the hindcast (red line). This cannot be linked to the limit of the original 3-hr resolution of the hindcast model. Wave buoy data recorded at Helgoland and resampled to the time resolution of the hindcast still shows the M2 peak.

6. Discussion

We investigated the characteristics of the microseism wavefield in the time interval 2004–2018 recorded at the 3C broadband island Station HLG in the North Sea. We evaluated the mean amplitude, the H/V ratios, and their temporal variability in the PMB, SMB, and LMB. These frequency bands were identified similarly to the global classifications in terms of identified energy peaks in the global new low noise model of Peterson (1993) and the observation of LM activity in the frequency range above 0.2 Hz (Cannata et al., 2019; Chen et al., 2011; Gal et al., 2015), respectively. We compared the results to time profiles of sea state, water level, air pressure, and recordings at additional seismic stations along the North Sea coast.

We identify contributions from RPM, RSM, LPM, and LSM to the microseismic wavefield at HLG. To identify the respective components of the wavefield, we use information about the frequency content, the SWH, and wave period at possible source regions and the H/V ratio in the investigated frequency band. As the dominant ocean wave period is determined by the extent of the sea area over which the wind can travel unobstructed and the duration of the maximum sustained wind speed (Bretschneider, 1959; Pierson & Moskowitz, 1964), open oceans with extended, well-developed storm systems like the North Atlantic are able to produce longer maximum wave periods than marginal seas with their limited extent like the North Sea. For this reason, dominant frequencies of RSM and RPM recorded at HLG are generally lower than the corresponding LSM and LPM signals (Figures 1 and 5). Although an amplification term related to local water

depth also needs to be taken into account to obtain the SM source term (e.g., Kedar et al., 2008), SWH by itself does work as a proxy for the strength of SM generation. An elevated sea state is needed to drive SM generation and is directly linked to high PM generation. A comparison of the dominant wave period recorded at a buoy in the vicinity of Helgoland shows that LSM and LPM frequencies observed at HLG are in agreement with recorded sea wave periods (Figures 5 and 8). The higher H/V ratio for signals interpreted as LPM is in agreement with former studies that found dominant Love wave contributions in the primary microseism noise field in Europe with Love-to-Rayleigh ratios of up to 2 (Juretzek & Hadziioannou, 2017). Depending on the ellipticity of the Rayleigh wave, this can result in H/V values of 3 or above comparable to values found in this study (Figure 8). On the other hand, secondary microseism mainly consists of fundamental mode Rayleigh waves (Gualtieri et al., 2013), and we thus expect a lower H/V ratio dominated by Rayleigh wave ellipticity for primary microseism. A study of the frequency-dependent fundamental mode Rayleigh wave ellipticity for a velocity model of the region of Helgoland (Figure S9) reveals only little variability in the considered frequency range. The velocity model used in the study was derived from seismic studies of Abramovitz et al. (1998, 1999) and the geotectonic atlas (GTA) for the German North Sea (Baldschuhn et al., 2001) and used the Computer Programs in Seismology software (Herrmann, 2013). For this reason, the exceptional high H/V variability cannot be explained in terms of an influence of fundamental mode Rayleigh wave ellipticity, and it seems to be caused more by additional Love wave contributions in LPM. The low H/V values (below 1) observed in the SMB during summer (Figure 8a) are also observed by Juretzek and Hadziioannou (2017) for a study using seismic arrays in Europe and have been interpreted as contribution of *P* waves from distant sources (possibly storms in the Southern Hemisphere as observed by Gerstoft et al., 2008, and Zhang et al., 2010). Below 0.1 Hz, the H/V value observed at HLG increases significantly. Considering the island location of station HLG, these high amplitudes related to tilt signals generated by seafloor deformation induced by ocean gravity waves (Crawford & Webb, 2000) are as expected strongest on the horizontal components. Young et al. (2013) identified foreshore loading and gravitational attraction from ocean swell and infragravity waves as causes of these tilt signals in a study of eight stations located within 100 m of the shoreline. Thus, the H/V value of RPM can not be estimated reliably in this study. While LSM has been described as short-period secondary microseism (SPSM) in former studies (Beucler et al., 2015; Chen et al., 2011), we also identify LPM in this marginal sea setting.

For LSM and LPM energy recorded at HLG, we observe clear spectral peaks in the diurnal, semidiurnal, and quarter-diurnal frequency ranges with the semidiurnal M2 partial tide being the most prominent peak (Figures 9 and 10). This peak also dominates the ocean tidal signal at HLG (Figure 11b) and throughout the North Sea and the North Atlantic in general. The rather high amplitude and the large number of quarter-diurnal tidal peaks observed at the tide gauge station at Helgoland (Figure 11c) is caused by multiples (overtides) or the superposition (compound tides) of the dominant ocean tidal frequencies (Dronkers, 1986; Friedrichs & Aubrey, 1988). These additional quarter-diurnal tidal peaks are caused by the asymmetry of the tides in shallow continental shelf areas altering the sinusoidal character of the tidal signal (Aubrey & Speer, 1985) and are especially pronounced in the shallow areas of the German Bight with average water depths below 30 m (Figure 2). This results in different periods for the tidal rise and fall and in consequence in different strengths of the ebb and flood currents as observed at tide gauge stations in the German Bight and at Helgoland (Figure 12a). The observation of these quarter-diurnal tidal frequencies in the microseism data (Figure 9d) suggests that the asymmetry in the ocean tides also influences to microseism energy generation.

Interestingly, also the SWH near Helgoland shows a clear temporal modulation with M2 and S2 (Figure 11e) and the shallow water tides M4 and MS4 (Figure 11f). This modulation is also visible in the time series of SWH shown in Figures 5 and 8. The maxima of water level and SWH coincide at Helgoland, as observed in former studies of tidal wave height modulation (Thomson et al., 2006). However, the elevated wave action during high tide, which Okihiro and Guza (1995) linked to the concave shape of the beach and thus different surf zone widths for a study in California, is not able to explain the observation at Helgoland. The rather small delay of 40 min between the maxima of the water level time derivative and the maximum energy in the LMB (Figure 12b) might hint at an influence of the currents in the LM generation. Because the derivative of the water level is only a rough estimate of the current velocity, it does not consider bathymetry; it might be possible that the maximum in current velocity is even closer to the maximum of LMB energy.

Young et al. (2013) found a 20° phase shift between water level maximum and maximum wave energy for a location on Hawaii and Dickson and Pentney (2012) observed highest wave activity and microseism energy during tidal lows at a location near Auckland, New Zealand. They explained this observation with a shore platform rising above water level during low tides. This indicates that the maximum of wave activity and microseism energy generation is not exclusively governed by water level but might in addition also depend on local bathymetry and currents as shown above.

The observation that tidal modulations of LMB energy are almost exclusively observed during times of local wave activity and/or tidal modulations of this wave activity (Figure S10) indicates that a combination of tidal currents and wave activity might be responsible for the increased LMB energy levels during rising tide. The interaction between tidal currents and ocean waves can lead to a steepening of waves and even breaking away from the coast when waves exceed their break criterion based on the steepness of the wave (Baschek, 2005). This mechanism can explain the general modulation of LMB energy with ocean tides. The observed time shift between the maximum in SWH and microseism energy (Figure 12b) hints at a generation region at some distance from the wave buoy registering the SWH. This discrepancy might be explained by the local variability in bathymetry and ocean currents.

For stations at the coast of Brittany (France), Beucler et al. (2015) also observed a strong tidal modulation of the microseism energy in the period range from 0.2–70 s. However, they observed no tidal modulation in the frequency range 0.2–0.4 Hz, which is prominent in our data, and explained this with the dominant influence of deep water generated SPSM at distances of several hundreds of kilometers. Young et al. (2013) also find strong tidal modulations of the microseism energy in the frequency range 0.01–0.1 Hz and at higher frequencies above 0.5 Hz. However, modulation in the frequency range between 0.2 and 0.5 Hz investigated in our study was only minor at the stations they studied in the Pacific and at the North Carolina coast. Thus, these former studies might have mainly registered the direct wave impact at the coast in the high-frequency region and the shoaling of swell and wind waves, that is, PM, in the lower frequency range below 0.2 Hz. In this study, however, we find pronounced tidal modulation for energy at double the dominant ocean wave frequency and thus strong tidal-modulated LSM near Helgoland and along the coast of the German Bight.

Most of the microseism amplitude spectrum peaks show a comparable amplitude ratio as the peaks found for the water level spectrum at Helgoland (Figures 11a–11c), indicating the ocean tidal control on the energy modulation. The only significant exception is in the diurnal period range, where the S1 peak is small compared with the K1 peak in the water level data, while it is exactly the opposite for the microseism data (Figure 11a). However, the S1 peak is prominently visible in the air pressure data (Figure 11g). We also observe a pronounced signal in the air pressure data at S2 (Figure 11h) corresponding to the strong microseism energy peak at this frequency. This might indicate an influence of the air pressure on the generation of LM at Helgoland and stresses the complex atmosphere/ocean/solid earth interaction responsible for the creation of ocean microseism.

An interpretation of the time shift between the maxima in LMB energy and water level and SWH by a LSM source off the coast of the Netherlands is incompatible with the results shown in Figure 13 where we observe a strong decrease of the tidal LM modulation with distance from the nearest shore (Figure 13a) and a time shift in the LMB energy maximum for stations along the North Sea coast that is matching the time shift of the tidal signal. It should be noted that this refers to the tidal signal at the seaward side of the Wadden Sea islands as the tidal signal at the actual coastline generally arrives with considerable delay. This is due to the exceptionally shallow Wadden Sea and the complexities caused by the islands (note, e.g., the time delay of 43 and 151 min, respectively, for two tide gauge stations toward the NW of seismic station SKMB; Figure 14). The observed phase shift in the maxima of LMB energy for stations along the North Sea thus suggests an origin of the LSM energy toward the seaward side of the islands in the German Bight. Furthermore, it suggests a distributed source region spanning the entire length of the German Bight. We find modulations of the sea state with the M2 tide for wave buoy measurements at locations seaward of the Wadden Sea islands (WEW1, HLG, and SYLT) and for one station (RZGN1) located between two islands at a location with exceptionally strong tidal dynamics due to the drainage of the river Ems into the North Sea. This tidal signal decreases with increasing distance from the shore as observed for stations with progressively larger distances from the island of Sylt (Figures 2 and 13d). Buoy FINO3 at a distance of about 70 km from the

nearest island shore shows no discernable signal. We thus suggest that the source region of the tide-modulated LSM signal may lie within a band of a few tens of kilometers seaward from the islands in the German Bight.

The local character of the LSM energy generation is further stressed by the fast decay of the signal with distance (Figures 13a and S8). For station BSEG at a distance of 90 km to the nearest North Sea coastline, no tidal modulation in the LMB is detectable (Figure 13a) and only weak LSM with lower frequencies can be recorded during elevated sea state in the North Sea (Figure S8b). For Station HLG, this suggests a source of the tidal-modulated LSM and LPM signal close to the island where tidal currents and the local sea state interact. To precisely pinpoint the source region, an array analysis resolving the exact source directions of LSM and LPM would be helpful. Furthermore, a spatially resolved map of the current sea state (in contrast to only point measurements by buoys) and a local wave model incorporating the influence of tidal currents could help identifying source regions. As obvious from Figure 13e, the used WAVEWATCH III[®] model does not contain any information on the tidal modulation of the sea state while the model output explains the general temporal behavior of the energy in the LMB quite well as evident in the high correlation coefficient (Figure 7a).

7. Conclusions

For the island Station HLG in the German Bight region of the southern North Sea RPM, RSM, LPM, and LSM contributions to the microseism wavefield were identified by means of their respective frequency content, the correlation with SWH in the vicinity of Helgoland and the North Atlantic, and their H/V value. While LSM dominates the wavefield in the LMB during the whole year, RSM is dominant in the SMB during winter. During quite sea states in the North Atlantic in summer, however, LPM can dominate the energy in the SMB with considerably higher H/V values than RSM. This indicates a considerable contribution of Love waves to LPM energy. Stable average H/V values of LSM during the whole year suggest a rather constant composition of the LMB wavefield during the whole year. RSM sources are found in the North Atlantic from the Norwegian coast up to the west of Ireland while LSM sources are identified in the Southern North Sea close to Helgoland.

A clear tidal modulation of LSM and LPM is found with peaks in the diurnal, semidiurnal, and quarter-diurnal frequency ranges also present in the water level and SWH data in the vicinity of Helgoland. This clearly suggests a tidal influence on the generation of microseism with the maximum in LSM and LPM energy preceding the maximum in sea level and wave activity at Helgoland. This might indicate an influence of the stronger tidal currents during rising tide on the generation of LSM and LPM.

The energy maximum in the LMB at stations along the coast of the North Sea migrates in lockstep with the tidal signal offshore the Wadden Sea islands. This indicates a migration of the LSM sources with the tidal signal in an anticlockwise motion along the North Sea.

The results of this study shed new light on the complexity of the microseism wavefield generated in marginal sea settings. Due to the generally highly diverse sea states in the North Sea and North Atlantic, the setting presented in this work allows a detailed analysis of LSM, LPM, RSM, and RPM often not possible at ocean sites with more homogeneous sea states. The observed strong tidal influence on the microseism energy generation makes it possible to identify potential source areas and might help in future studies in the identification of the remote sea state when the tidal dynamics is known or vice versa. This study also sets the basis for further investigations focused on the identification of generation conditions of LSM and LPM and might give insight into the generation of Love waves in LPM that are the primary candidate of their characteristically higher H/V ratios.

To further improve the understanding of LM in a marginal sea setting like the North Sea, it is necessary to better constrain the exact source areas of LPM and LSM and to investigate the possible contributions of air pressure, ocean currents, and bathymetry on microseism generation. This requires a highly multidisciplinary approach with multiparameter stations within the study region investigating the complex atmosphere/ocean/solid-earth interactions and linking the fields of seismology, atmospheric science, oceanography, and marine seismics.

Data Availability Statement

Data of significant wave height and water level are provided by Bundesamt für Seeschifffahrt und Hydrographie (BSH) through the North West Shelf Data Portal (<http://nwsportal.bsh.de>). Air pressure data are provided by Deutscher Wetterdienst (DWD, https://opendata.dwd.de/climate_environment/CDC/observations_germany/climate/hourly/pressure/historical/), and model outputs from the WAVEWATCH III® models can be obtained from the National Weather Service's National Centers for Environmental Prediction (NCEP) at the National Oceanographic and Atmospheric Administration (NOAA, ftp://polar.ncep.noaa.gov/pub/history/waves/multi_1/). Figures 1, 2, and 14 were created using GMT v5.2.1 (Wessel et al., 2013), bathymetry in Figures 2 and 14 was obtained from EMODnet (<https://portal.emodnet-bathymetry.eu/>), and bathymetry in Figure 1 from the ETOPO1 Global Relief model (<https://www.ngdc.noaa.gov/mgg/global/>, <http://10.7289/V5C8276M>). The data processing routines have been written in MATLAB (2018).

Acknowledgments

We thank the Associate Editor Nori Nakata and two anonymous reviewers for their critical and constructive suggestions that significantly helped to improve the manuscript. Station HLG is part of the GEOFON network (<https://doi.org/10.14470/TR560404>) of the GeoForschungs-Zentrum Potsdam (GFZ, <https://geofon.gfz-potsdam.de>). Stations IGAD, BSEG, and SKMB are part of the German Regional Seismic Network (GRSN, <https://doi.org/10.25928/mbx6-hr74>) of the Bundesanstalt für Geowissenschaften und Rohstoffe (BGR, <https://eida.bgr.de>). Station G021 is part of the Netherlands Seismic and Acoustic network (<https://doi.org/10.21944/e970fd34-23b9-3411-b366-e4f72877d2c5>) of the Koninklijk Nederlands Meteorologisch Instituut (KNMI, <http://rdsa.knmi.nl>).

References

- Abramovitz, T., Landes, M., Thybo, H., Jacob, A. W. B., & Prodehl, C. (1999). Crustal velocity structure across the Tornquist and Iapetus suture zones—A comparison based on MONA LISA and VARNET data. *Tectonophysics*, *314*(1–3), 69–82. [https://doi.org/10.1016/S0040-1951\(99\)00237-1](https://doi.org/10.1016/S0040-1951(99)00237-1)
- Abramovitz, T., Thybo, H., & MONA LISA working group (1998). Seismic structure along the Caledonian deformation front along MONA LISA profile 1 in the southeastern North Sea. *Tectonophysics*, *288*, 153–176. [https://doi.org/10.1016/S0040-1951\(97\)00290-4](https://doi.org/10.1016/S0040-1951(97)00290-4)
- Ardhuin, F. (2018). Large-scale forces under surface gravity waves at a wavy bottom: A mechanism for the generation of primary microseisms. *Geophysical Research Letters*, *45*, 8173–8181. <https://doi.org/10.1029/2018GL078855>
- Ardhuin, F., Gualteri, L., & Stutzmann, L. (2015). How ocean waves rock the Earth: Two mechanisms explain microseisms with periods 3 to 300 s. *Geophysical Research Letters*, *42*, 765–772. <https://doi.org/10.1002/2014GL062782>
- Aubrey, D. G., & Speer, P. E. (1985). A study of non-linear tidal propagation in shallow inlet/estuarine systems. Part I: Observations. *Estuarine Coastal and Shelf Science Journal*, *21*(2), 185–205. [https://doi.org/10.1016/0272-7714\(85\)90096-4](https://doi.org/10.1016/0272-7714(85)90096-4)
- Baldschuhn, R., Binot, F., Fleig, S., & Kockel, F. (2001). Geotektonischer Atlas von Nordwestdeutschland und dem deutschen Nordsee-Sektor. In *Geologisches Jahrbuch* (Vol. A153, pp. 1–88). Stuttgart, Germany: Schweizerbart Science Publishers.
- Baschek, B. (2005). Wave-current interaction in tidal fronts. In R. Waves, P. Müller, C. Garrett (Eds.), *Proceedings 14th 'Aha Huliko' a Winter Workshop 2005: Rouge Waves* (pp. 131–138). Honolulu, USA.
- Beucler, É., Mocquet, A., Schimmel, M., Chevrot, S., Quillard, O., Vergne, J., & Sylvander, M. (2015). Observation of deep water microseisms in the North Atlantic Ocean using tide modulations. *Geophysical Research Letters*, *42*, 316–322. <https://doi.org/10.1002/2014GL062347>
- Bretschneider, C. L. (1959). Wave variability and wave spectra for wind-generated gravity waves. *Beach Erosion Board, Office of the Chief of Engineers, U.S. Army*. Technical Memorandum No. 118, 122pp. Washington, DC.
- Bromirski, P., & Duennebieber, F. (2002). The near-coastal microseism spectrum: Spatial and temporal wave climate relationships. *Journal of Geophysical Research*, *107*(B8), 2166. <https://doi.org/10.1029/2001JB000265>
- Cannata, A., Cannavò, F., Moschella, S., Gresta, S., & Spina, L. (2019). Exploring the link between microseism and sea ice in Antarctica by using machine learning. *Scientific Reports*, *9*(1), 13050. <https://doi.org/10.1038/s41598-019-49586-z>
- Cessaro, R. K. (1994). Sources of primary and secondary microseisms. *Bulletin of the Seismological Society of America*, *84*(1), 142–148.
- Chawla, A., Spindler, D. M., & Tolman, H. L. (2013). Validation of a thirty year wave hindcast using the climate forecast system reanalysis winds. *Ocean Modelling*, *70*, 189–206. <https://doi.org/10.1016/j.ocemod.2012.07.005>
- Chen, Y.-N., Gung, Y., You, S.-H., Hung, S.-H., Chiao, L.-Y., Huang, T.-Y., et al. (2011). Characteristics of short period secondary microseisms (SPSM) in Taiwan: The influence of shallow ocean strait on SPSM. *Geophysical Research Letters*, *38*, L04305. <https://doi.org/10.1029/2010GL046290>
- Crawford, W. C., & Webb, S. C. (2000). Identifying and removing tilt noise from low-frequency (<0.1 Hz) seafloor vertical seismic data. *Bulletin of the Seismological Society of America*, *90*(4), 952–963. <https://doi.org/10.1785/0119990121>
- Dickson, M. E., & Pentney, R. (2012). Micro-seismic measurements of cliff motion under wave impact and implications for the development of near-horizontal shore platforms. *Geomorphology*, *151–152*, 27–38. <https://doi.org/10.1016/j.geomorph.2012.01.006>
- Dolenc, D., Romanowicz, B., Stakes, D., McGill, P., & Neuhauser, D. (2005). Observations of infragravity waves at the Monterey ocean bottom broadband station (MOBB). *Geochemistry, Geophysics, Geosystems*, *6*, Q09002. <https://doi.org/10.1029/2005GC000988>
- Dronkers, J. (1986). Tidal asymmetry and estuarine morphology. *Netherlands Journal of Sea Research*, *20*(2–3), 117–131. [https://doi.org/10.1016/0077-7579\(86\)90036-0](https://doi.org/10.1016/0077-7579(86)90036-0)
- Essen, H.-H., Klusmann, J., Herber, R., & Grevemeyer, I. (1999). Do microseisms in Hamburg (Germany) reflect the wave climate in the North Atlantic? *Deutsche Hydrographische Zeitschrift*, *51*(1), 33–45. <https://doi.org/10.1007/BF02763955>
- Friedrich, A., Krüger, F., & Klinge, K. (1998). Ocean-generated microseismic noise located with the Gräfenberg array. *Journal of Seismology*, *2*(1), 47–64. <https://doi.org/10.1023/A:1009788904007>
- Friedrichs, C. T., & Aubrey, D. G. (1988). Non-linear tidal distortion in shallow well-mixed estuaries: A synthesis. *Estuarine, Coastal and Shelf Science*, *27*, 521–545. [https://doi.org/10.1016/0272-7714\(88\)90082-0](https://doi.org/10.1016/0272-7714(88)90082-0)
- Gal, M., Reading, A. M., Ellingsen, S. P., Gualtieri, L., Koper, K. D., Burlacu, R., et al. (2015). The frequency dependence and locations of short-period microseisms generated in the Southern Ocean and West Pacific. *Journal of Geophysical Research: Solid Earth*, *120*, 5764–5781. <https://doi.org/10.1002/2015JB012210>
- Gerstoft, P., Shearer, P. M., Harmon, N., & Zhang, J. (2008). Global P, PP, and PKP wave microseisms observed from distant storms. *Geophysical Research Letters*, *35*, L23306. <https://doi.org/10.1029/2008GL036111>
- Grevemeyer, I., Herber, R., & Essen, H.-H. (2000). Microseismological evidence for a changing wave climate in the Northeast Atlantic Ocean. *Nature*, *408*(6810), 349–352. <https://doi.org/10.1038/35042558>

- Gualtieri, L., Stutzmann, E., Capdeville, Y., Arduin, F., Schimmel, M., Mangeny, A., & Morelli, A. (2013). Modelling secondary microseismic noise by normal mode summation. *Geophysical Journal International*, *193*(3), 1732–1745. <https://doi.org/10.1093/gji/ggt090>
- Hasselmann, K. (1963). A statistical analysis of the generation of microseisms. *Reviews of Geophysics*, *1*(2), 177–210. <https://doi.org/10.1029/RG001i002p00177>
- Herrmann, R. B. (2013). Computer programs in seismology: An evolving tool for instruction and research. *Seismological Research Letters*, *84*(6), 1081–1088. <https://doi.org/10.1785/0220110096>
- Hillers, G., Graham, N., Campillo, M., Kedar, S., Landès, M., & Shapiro, N. (2012). Global oceanic microseism sources as seen by seismic arrays and predicted by wave action models. *Geochemistry Geophysics Geosystems*, *13*, Q01021. <https://doi.org/10.1029/2011GC003875>
- Juretzek, C., & Hadziioannou, C. (2016). Where do ocean microseism come from? A study of Love-to-Rayleigh wave ratios. *Journal of Geophysical Research: Solid Earth*, *121*, 6741–6756. <https://doi.org/10.1002/2016JB013017>
- Juretzek, C., & Hadziioannou, C. (2017). Linking source region and ocean wave parameters with the observed primary microseismic noise. *Geophysical Journal International*, *211*(3), 1640–1654. <https://doi.org/10.1093/gji/ggx388>
- Kedar, S., Longuet-Higgins, M., Webb, F., Graham, N., Clayton, R., & Jones, C. (2008). The origin of deep ocean microseisms in the North Atlantic Ocean. *Proceedings of the Royal Society A: Mathematical Physical and Engineering Sciences*, *464* (2091), 777–793 <https://doi.org/10.1098/rspa.2007.0277>, 2091
- Kendall, M. G. (1970). *Rank correlation methods*. London: Griffin.
- Lin, F.-C., Moschetti, M. P., & Ritzwoller, M. H. (2008). Surface wave tomography of the western United States from ambient seismic noise: Rayleigh and Love wave phase velocity maps. *Geophysical Journal International*, *173*(1), 281–298. <https://doi.org/10.1111/j.1365-246X.2008.03720.x>
- Longuet-Higgins, M. S. (1950). A theory of the origin of microseisms. *Philosophical Transactions of the Royal Society of London Series A, Mathematical and Physical Sciences*, *243*(857), 1–35. <https://doi.org/10.1098/rsta.1950.0012>
- MATLAB (2018). *Matlab version 9.4.0.813654 (R2018a)*. Natick, Massachusetts: The Mathworks, Inc.
- McNamara, D. E., & Buland, R. P. (2004). Ambient noise levels in the continental United States. *Bulletin of the Seismological Society of America*, *94*(4), 1517–1527. <https://doi.org/10.1785/012003001>
- Nishida, K., Kawakatsu, H., Fukao, Y., & Obara, K. (2008). Background Love and Rayleigh waves simultaneously generated at the Pacific Ocean floors. *Geophysical Research Letters*, *35*, L16307. <https://doi.org/10.1029/2008GL034753>
- Okiihiro, M., & Guza, R. T. (1995). Infragravity energy modulation by tides. *Journal of Geophysical Research*, *100*(C8), 16,143–16,148. <https://doi.org/10.1029/95JC01545>
- Peterson, J. R. (1993). Observation and modeling of seismic background noise. *U.S. Geological Survey Technical Report*, 93–322, 1–95. <https://doi.org/10.3133/ofr93322>
- Pierson, W. J. Jr., & Moskowitz, L. A. (1964). Proposed spectral form for fully developed wind seas based on the similarity theory of S. A. Kitaigorodskii. *Journal of Geophysical Research*, *69*(24), 5181–5190. <https://doi.org/10.1029/JZ069i024p05181>
- Sutton, G., & Barstow, N. (1996). Ocean bottom microseisms from a distant supertyphoon. *Geophysical Research Letters*, *23*(5), 499–502. <https://doi.org/10.1029/96GL00419>
- Tanimoto, T., & Alvizuri, C. (2006). Inversion of the HZ ratio of microseisms for S-wave velocity in the crust. *Geophysical Journal International*, *165*(1), 323–335. <https://doi.org/10.1111/j.1365-246X.2006.02905.x>
- Thomson, J., Elgar, S., Raubenheimer, B., Herbers, T. H. C., & Guza, R. T. (2006). Tidal modulation of infragravity waves via nonlinear energy losses in the surfzone. *Geophysical Research Letters*, *33*, L05601. <https://doi.org/10.1029/2005GL025514>
- Tolman, H. L. (2009). *User manual and system documentation of WAVEWATCH III® version 3.14*. Tech. Note 276 (p. 220). Camp Springs, MD: NOAA/NWS/NCEP/MMAB.
- Traer, J., Gerstoft, P., Bromirski, P., Hodgekiss, W., & Brooks, L. (2008). Shallow-water seismoacoustic noise generated by tropical storms Ernesto and Florence. *The Journal of the Acoustical Society of America*, *124*(3), EL170–EL176. <https://doi.org/10.1121/1.2968296>
- Webb, S. C. (1998). Broadband seismology and noise under the ocean. *Reviews of Geophysics*, *36*(1), 105–142. <https://doi.org/10.1029/97RG02287>
- Wessel, P., Smith, W. H. F., Scharroo, R., Luis, J. F., & Wobbe, F. (2013). Generic Mapping Tools: Improved version released. *Eos, Transactions of the American Geophysical Union*, *94*(45), 409–410. <https://doi.org/10.1002/2013EO450001>
- Young, A., Guza, R., Dickson, M., O'Reilly, W., & Flick, R. (2013). Ground motions on rocky, cliffed, and sandy shorelines generated by ocean waves. *Journal of Geophysical Research: Oceans*, *118*, 6590–6602. <https://doi.org/10.1002/2013JC008883>
- Zhang, J., Gerstoft, P., & Bromirski, P. D. (2010). Pelagic and coastal sources of P-wave microseisms: Generation under tropical cyclones. *Geophysical Research Letters*, *37*, L15301. <https://doi.org/10.1029/2010GL044288>